Acoustic Wave Propagation and its Application to Fluid Structure Interaction using the Cumulant Lattice Boltzmann Method

Mohsen Gorakifard[a], Ildefonso Cuesta[a], Clara Salueña[a,*], Ehsan Kian Far[b]

[a]Department of Mechanical Engineering, ETSEQ, Rovira i Virgili University, Països Catalans, 26, 43007, Tarragona, Spain
[b]Department of Chemical Engineering & Analytical Science,The University of Manchester, The Mill, Manchester M1 3AL, United Kingdom

Abstract

Splitter plates attached to a cylinder looking like hair (SPCH) is one of the self-adaptive devices used to control actual flow conditions, which in turn interact with Aeolian tones constituting a typical case of study in engineering industries. The direct numerical simulation of the sound waves stimulated by such devices is a complicated task due to the small levels of sound pressure and the time-consuming existing solvers. However, the Cumulant Lattice Boltzmann Method (LBM) provides stability and robustness at high Reynolds numbers and carries out these simulations satisfactorily. First, the fundamental acoustical properties of the Cumulant LBM are studied in this paper. Propagation of point and planar acoustic waves is considered including the temporal decay of a standing plane wave, the spatial decay of a planar acoustic pulse, and the propagation of spherical waves. Then, the Cumulant LBM as a fluid flow solver is coupled with a Finite Element structural mechanics solver to predict the effects of SPCH on the noise generated by cylinders at high Reynolds numbers as a practical fluid structure interaction (FSI) application. The spectral modification and possible acoustic damping impact of such flaps, plus the sound propagation from one and two circular cylinders are studied. A comparison of the theoretical and numerical results shows a reasonable capability of the Cumulant LBM to predict acoustical events with small errors in dissipation and dispersion. Furthermore, the results show that SPCH alter the phase of the vortex shedding cycle and decrease the transversal distance from the center line of the shed vortices. Flaps, thus, control the wake generated past a cylinder and have an effective impact on decreasing sound generation.

Keywords: Acoustics; Aeolian Tones; Cumulant LBM; Finite Element Method; Fluid Structure Interaction;

*Corresponding author
Email address: clara.saluena@urv.cat (Clara Salueña)

1. Introduction

Noise reduction is an important part of engineering design in transportation industries such as aircraft, high speed trains, automobiles, and so on. In general, noise limits engine operation, disturbs passengers and operators, and pollutes the environment. As a result, the understanding and controlling of noise is fundamental.

A typical case of aerodynamic noise is the Aeolian tone, named after the god of winds Aeolus in the Hellenic mythology. The first observations of Aeolian tones [1, 2, 3] were made in sound generated from bluff bodies like cylinders immersed in a flow [4, 5]. Researchers believe that the hydrodynamic instability of the wake behind a cylinder after a specific critical Reynolds number, results in sound with strong tonal components based on the vortex shedding frequency. Strouhal's studies on the existence of these vortex shedding tones [6] lead to the non-dimensional Strouhal number, which is the relation between the frequency of the vortex shedding tone, the characteristic length, and the free stream velocity.

Hardin et al. [7] calculated the sound generated by an incompressible and time dependent flow over a cylinder at low Reynolds numbers. Cox et al. [8] studied the tonal noise generated from a circular cylinder for a wide range of Reynolds numbers, and compared with experimental studies. In addition, Inoue et al. [9] simulated the sound generated by two squares at a Mach number equal of 0.2 using direct solution of the 2D unsteady compressible Navier-Stokes equations. Tam [10] and Wells et al. [11] studied different popular numerical schemes in the the field of computational aeroacoustics (CAA). They presented compact and non-compact optimized schemes which are mostly based on linear wave propagation, such as the high-order compact difference schemes [12, 13] and the dispersion-relation-preserving (DRP) scheme [14]. Among these methods, the DRP scheme is the most simple thanks to the use of symmetric finite differences on uniform Cartesian grids. To simulate curvilinear problems in aeroacoustics, grid-optimized dispersion-relation-preserving (GODRP) schemes were developed [15]. However, the prediction of aerodynamic noise is burdensome because of the huge cost of CAA simulations, which resulted in developing hybrid methods. Hybrid methods use two sets of equations, one for the flow and another one for the acoustic disturbance field.

To control the flow and sound side effects, self-adaptive devices can be utilized. The devices for manipulating vortex shedding play a critical role in many engineering problems. As an illustration, splitter plates have been known as one of the effective ways for controlling vortex shedding [16, 17]. Recently, several investigations have been carried out on the effect of an attached rigid splitter plate on the flow pattern behind a cylinder [18, 19, 20]. They showed that the length of the splitter plate strongly influences the

character of the vortex shedding for different fluid flow regimes. Mazellier et al. [21] studied flexible membranes, similar to bird's feathers, to control the flow behind a square. Brucker et al. experimentally studied the effects of flexible flaps on the flow around a cylinder. They showed that flaps can alter the shedding cycle [22, 23]. In addition, the motion pattern of the flaps changes to a wavy shape when the amplitude is increased beyond some specific Reynolds. As a result, the vortices transversal distance from the center line, structural vibrations, and sound generation decrease.

The direct numerical simulation of sound waves stimulated by controlling devices is complicated since the sound pressure is much smaller than the whole pressure variation. In addition, the acoustic field spreads in large regions and this is a time-consuming process. For example, the direct numerical simulation of sound waves based on Navier-Stokes equations needs schemes of fifth-order accuracy in space and fourth-order accuracy in time [24, 25, 26]. On the other hand, the Lattice Boltzmann method (LBM) is a new and reliable method of computational fluid dynamics (CFD) which has been developed from the lattice gas method and can be used as an alternative to simulate sound wave propagation. Furthermore, the coupling of the LB method with the finite element method is relatively straightforward. Generally, the LB method, an explicit time marching scheme, is used for a broad category of advection-diffusion problems [27].

The LBM has been widely used in many applications in the field of acoustics. Buick et al. [29] and Dellar et al.[30] studied sound wave propagation using LBM, achieving acceptable results. Crouse et al. [31] investigated the propagation of standing acoustic waves and showed that the LBM can yield relatively good results on fundamental acoustic phenomena. Mari´e et al. [32] and Bres et al. [33] presented the dissipation and dispersion of acoustic waves using the BGK-LBM. Viggen [34] proposed the sound propagation properties of the lattice Boltzmann equation for both free and forced waves. In addition, he proposed an extended model containing a bulk viscosity correction term with the idea that all equilibrium distributions must be identical for the one-dimensional D1Q3 velocity set. Dhuri et al. [35] investigated linear acoustic wave propagation in heterogeneous media with the BGK approximation and the multi-relaxation-time collision operators for the D2Q5 model. It should be noticed that many different schemes have been used because of numerical instabilities appearing when dealing with high Reynolds numbers [36, 37, 38] or specific characteristics of the fluid: the Taylor expansion method [39], the dual entropy approach [40], the local/global lower bound on the relaxation time [41], selective viscosity filtering [42], dissipation/dispersion optimized multiple relaxation times [43, 44, 45], augmenting hyper-viscosities in non-uniform grids [46, 47, 48], the entropy H-theorem [49, 50, 51, 52], a regularized method for the BGK-LBM [53], the recursive and regularized LBM (LBM-rrBGK) [54, 55], and the Cumulant LBM [56, 57, 58, 59]. The recursively regularized LBM has been

recently expanded and used for isothermal and weakly compressible flows at high Reynolds numbers, and fully compressible flows [60, 61, 62]. Among these schemes, all of them having advantages and disadvantages, here the Cumulant LBM is chosen due to the number of existing studies in the field of acoustics. Therefore, the aim of this paper is to study the capability of the Cumulant LBM to simulate sound wave propagation by calculating the deviation from analytical results, notably the dissipation and dispersion errors. Moreover, it tries to assess the effects of SPCH at high velocities on the noise beyond the cylinders, particularly, the acoustic damping effect of such flaps on sound propagation through interactions among acoustic waves, solid walls and shear layers.

2. Methodology

To study the effects of SPCH on the fluid domain and sound wave propagation, this section presents an explanation of the mathematics behind this complex phenomenon. First, the general description of the Cumulant Lattice Boltzmann method as a flow field solver is provided. Second, the finite element system of equations derived for the structural solver and the Newmark Method is explained. Then, details on the fluid structure coupling are considered. Finally, to examine the results of the Cumulant LBM for the wave propagation, the general form of the lossy wave equation is obtained.

2.1. Cumulant Lattice Boltzmann

The Lattice Boltzmann method (LBM), a suitable substitute for Navier-Stokes solvers, can simulate complex fluid flow. This mesoscopic method is obtained from Ludwig Boltzmann's kinetic theory of gases. Although the LBM is regarded as a finite difference method for solving the Boltzmann transport equation, it leads to the Navier-Stokes equations by using the Chapman-Enskog expansion. The basic idea is that gas or fluid motion is modeled by a discrete momentum distribution function, to transfer momentum and energy through particle streaming and billiard-like particle collision on a Cartesian grid, at each time step [27]. In general, the lattice is denoted by DdQq where d and q are the number of dimension and the number of the discrete speeds, respectively. The lattice Boltzmann equation without an external force is

$$f_i\left(x + e_{xi}c\Delta t, y + e_{yi}c\Delta t, t + \Delta t\right) - f_i\left(x, y, t\right) = \Omega_i \tag{1}$$

where f_i, Ω_i and $c = \Delta x/\Delta t$ are the particle distribution function, the collision operator and the lattice speed, respectively.

In general, the LBM contains two key steps: collision and streaming. The most difficult part of the LBM solving the collision term, and different choices give rise to methods like BGK, MRT, Cascade, Cumulant, and so on. This paper considers the Cumulant method as one of the newest and most robust LB methods.

The probability density function (PDF) is [28]

$$\boldsymbol{f}(\xi,\eta) = \sum_{ij} f(\xi_i,\eta_j)\delta(\xi-\xi_i)\delta(\eta-\eta_i), \tag{2}$$

where f is the probability mass function (PMF) and ξ,η are discrete random variables with ranges $R_\xi = \{\xi_1,\xi_2,\ldots\}$, $R_\eta = \{\eta_1,\eta_2,\ldots\}$ corresponding to the microscopic velocities in x, y directions.

The moments of such PDF, without any discontinuity problems can be calculated as

$$\mu'_{\xi^m\eta^n} = \frac{\partial^m\partial^n}{\partial\Xi^m\partial\mathrm{H}^n} M(\Xi,\mathrm{H})\Big|_{\Xi=\mathrm{H}=0}, \tag{3}$$

where $M(\Xi,\mathrm{H}) = \sum_{ij} f(\xi_i,\eta_j)e^{\Xi\xi_i}e^{\mathrm{H}\eta_j}$ is the moment generating function and H, Ξ are the normalized wave numbers.

To reduce the Galilean invariant problems of the collision step, the moment generating function is shifted into the moving frame of reference of the fluid. Then, the central moments can be calculated as

$$\mu_{\xi^m\eta^n} = \frac{\partial^m\partial^n}{\partial\Xi^m\partial\mathrm{H}^n} \widehat{M}(\Xi,\mathrm{H})\Big|_{\Xi=\mathrm{H}=0} \tag{4}$$

where $\widehat{M}(\Xi,\mathrm{H}) = e^{-\Xi u/c-\mathrm{H}v/c}M(\Xi,\mathrm{H})$ is the central moment generating function.

To use the advantage of the logarithmic form of the moment generating function, the cumulant generating function is defined as [63]

$$c_{\xi^m\eta^n} = \frac{\partial^m\partial^n}{\partial\Xi^m\partial\mathrm{H}^n} \ln(M(\Xi,\mathrm{H}))\Big|_{\Xi=\mathrm{H}=0}. \tag{5}$$

Each cumulant relaxes with an individual relaxation rate

$$c^*_{\xi^m\eta^n} = c_{\xi^m\eta^n} + \omega_{\xi^m\eta^n}(c^{eq}_{\xi^m\eta^n} - c_{\xi^m\eta^n}) \tag{6}$$

where $c^{eq}_{\xi^m\eta^n}$ are the cumulants of the equilibrium state. The equilibrium state for the cumulant generating function is $CGF^{eq} = \Xi u/c + \mathrm{H}v/c + \frac{\varsigma^2(\Xi^2+\mathrm{H}^2)}{2c^2}$ [64]. The sound speed and the kinematic viscosity are calculated respectively, [65]

$$\varsigma_s = \frac{\Delta x}{\sqrt{3}\Delta t}, \tag{7}$$

$$\nu = \Delta t \varsigma^2 (\frac{1}{\omega} - \frac{1}{2}). \tag{8}$$

To itemize the algorithm: First the central moments of the distribution function are calculated using equation (4). Second, the cumulants are obtained from the central moments. Third, the post-collision cumulants from the collision operator are quantified based on equation (6). Fourth, post-collision central moments from the post-collision cumulants are extracted. Fifth, the post-collision central moments are transferred back to the distribution functions [27].

2.2. Structural analysis

One of the numerical methods to simulate structural phenomena, is the finite element method (FEM). The FEM, generally, describes a set of algebraic equations for a domain subdivided into small-interconnected parts called finite elements. The elements are linked together by common interfaces, containing nodes, boundary lines, and surfaces. In this study the Euler-Bernoulli beam is used as structure. The transverse deflection w of the beam is governed by

$$\frac{d^2}{dx^2}\left(b\frac{d^2w}{dx^x}\right) = f(x), \qquad 0 < x < L \tag{9}$$

where $b = b(x)$, $f = f(x)$, and f is the transversely distributed load. The function $b = EI$ where E is the elasticity modulus and I is the moment of inertia. Equation (9) needs four boundary conditions. The structural domain is divided into a set of N line elements. To derive the element equations [66], a typical element $\Omega^e = (x_e, x_{e+1})$ is isolated and the weak form of equation (9) over this element is constructed as

$$\begin{aligned} 0 &= \int_{x_e}^{x_{e+1}} v\left[\frac{d^2}{dx^2}\left(b\frac{d^2w}{dx^2}\right) - f\right]\mathrm{d}x \\ &= \int_{x_e}^{x_{e+1}}\left[-\frac{dv}{dx}\frac{d}{dx}\left(b\frac{d^2w}{dx^2}\right) - vf\right]\mathrm{d}x + \left[v\frac{d}{dx}\left(b\frac{d^2w}{dx^2}\right)\right]_{x_e}^{x_{e+1}} \\ &= \int_{x_e}^{x_{e+1}}\left(b\frac{d^2v}{dx^2}\frac{d^2w}{dx^2} - vf\right)\mathrm{d}x + \left[v\frac{d}{dx}\left(b\frac{d^2w}{dx^2}\right) - \frac{dv}{dx}b\frac{d^2w}{dx^2}\right]_{x_e}^{x_{e+1}} \end{aligned} \tag{10}$$

where $v(x)$ is a weight function. Due to the two integrations by parts, an examination of the boundary terms makes it clear that the essential boundary conditions involve the deflection w and its derivative dw/dx, whereas the natural boundary conditions involve the bending moment bd^2w/d^2 and the shear force $(d/dx)(bd^2w/dx^2)$ at the endpoint of the element. Using the following notation,

$$\begin{aligned}
\theta &= -\frac{dw}{dx}, \\
\Phi_1^e &\equiv \left[\frac{d}{dx}\left(b\frac{d^2w}{dx^2}\right)\right]_{x_e}, \quad \Phi_2^e \equiv \left(b\frac{d^2w}{dx^2}\right)\Big|_{x_e}, \\
\Phi_3^e &\equiv -\left[\frac{d}{dx}\left(b\frac{d^2w}{dx^2}\right)\right]_{x_{e+1}}, \quad \Phi_4^e \equiv -\left(b\frac{d^2w}{dx^2}\right)\Big|_{x_{e+1}},
\end{aligned} \tag{11}$$

equation (10) results in

$$0 \equiv B(v,w) - L(v) \tag{12}$$

$$\begin{aligned}
B(v,w) &= \int_{x_e}^{x_{e+1}} b\frac{d^2v}{dx^2}\frac{d^2w}{dx^2}\,\mathrm{d}x, \\
L(v) &= \int_{x_e}^{x_{e+1}} vf\,\mathrm{d}x + v(x_e)\Phi_1^e + \left(-\frac{dv}{dx}\right)\Big|_{x_e} + \Phi_2^e + v(x_{e+1})\Phi_3^e + \left(-\frac{dv}{dx}\right)\Big|_{x_{e+1}}\Phi_4^e,
\end{aligned}$$

which is a statement of the principle of virtual displacements, known as total potential energy of the beam element. Equation (12) requires interpolation functions (ϕ) for the element, which are continuous with nonzero derivatives up to order two. By satisfying the interpolation properties the functions are calculated as

$$w^e(x) = u_1^e\phi_1^e + u_2^e\phi_2^e + u_3^e\phi_3^e + u_4^e\phi_4^e = \sum_{j=1}^{4} u_j^e\phi_j^e, \tag{13}$$

$$\begin{aligned}
&u_1^e = w(x_e), \quad u_2^e = \theta|_{x_e}, \quad u_3^e = w(x_{e+1}), \quad u_4^e = \theta|_{x_{e+1}}, \\
&\phi_1^e = 1 - 3\left(\frac{x-x_e}{h_e}\right)^2 + 2\left(\frac{x-x_e}{h_e}\right)^3, \quad \phi_2^e = -(x-x_e)\left(1 - \frac{x-x_e}{h_e}\right)^2, \\
&\phi_3^e = 3\left(\frac{x-x_e}{h_e}\right)^2 - 2\left(\frac{x-x_e}{h_e}\right)^3, \quad \phi_4^e = -(x-x_e)\left[\left(\frac{x-x_e}{h_e}\right)^2 - \frac{x-x_e}{h_e}\right].
\end{aligned}$$

The finite element model is calculated by substituting w from (13) and $v = \phi_i$ into equation (12),

$$K_{ij}^{x_{e+1}} = \int_{x_e}^{x_{e+1}} b \frac{d^2\phi_i^e}{dx^2} \frac{d^2\phi_j^e}{dx^2} \, \mathrm{d}x, \tag{14}$$

$$F_i^{x_{e+1}} = \int_{x_e}^{x_{e+1}} \phi_i^e f \, \mathrm{d}x + \Phi_i^e, \tag{15}$$

$$\sum_{j=1}^{4} K_{ij}^e u_j^e - F_i^e = 0. \tag{16}$$

To obtain the time-dependent form of the equation of motion, the mass matrix is calculated as [67]

$$M_{ij}^e = \int_{x_e}^{x_{e+1}} m\phi_i^e \phi_j^e \, \mathrm{d}x. \tag{17}$$

And with the same $b = EI$, the matrix elements of M, K, and F are

$$K^e = \frac{EI}{h} \begin{bmatrix} \frac{12}{h^2} & \frac{-6}{h} & \frac{-12}{h^2} & \frac{-6}{h} \\ \frac{-6}{h} & 4 & \frac{6}{h} & 2 \\ \frac{-12}{h^2} & \frac{6}{h} & \frac{12}{h^2} & \frac{6}{h} \\ \frac{-6}{h} & 2 & \frac{6}{h} & 4 \end{bmatrix}, \quad F^e = -\frac{fh}{12} \begin{bmatrix} 6 \\ -h \\ 6 \\ h \end{bmatrix} + \begin{bmatrix} \Phi_1 \\ \Phi_2 \\ \Phi_3 \\ \Phi_4 \end{bmatrix}, \quad M^e = mh \begin{bmatrix} \frac{13}{35} & h\frac{11}{210} & \frac{9}{70} & -h\frac{13}{420} \\ h\frac{11}{210} & h\frac{1}{105} & h\frac{13}{420} & -h\frac{1}{140} \\ \frac{9}{70} & h\frac{13}{420} & \frac{13}{35} & -h\frac{11}{210} \\ -h\frac{13}{420} & -h\frac{1}{140} & -h\frac{11}{210} & h\frac{1}{105} \end{bmatrix}. \tag{18}$$

The governing equation for the linear dynamic response of the finite element system is

$$M\ddot{\boldsymbol{x}} + C\dot{\boldsymbol{x}} + K\boldsymbol{x} = F, \tag{19}$$

where M, C, K are the mass, damping, and stiffness matrices. F is the external force vector and $\boldsymbol{x}$ is the displacement vector [68].

The discrete equation system (19) is solved using the Newmark method, which is a direct integration method [68]. In this paper, the standard Newmark method is used as follows. It is first assumed that

$$\boldsymbol{x}_{t+\Delta t} = \boldsymbol{x}_t + (\Delta t)\dot{\boldsymbol{x}}_t + (\Delta t)^2 \left[(0.5 - \beta)\ddot{\boldsymbol{x}}_t + \beta\ddot{\boldsymbol{x}}_{t+\Delta t}\right], \tag{20a}$$

$$\dot{\boldsymbol{x}}_{t+\Delta t} = \dot{\boldsymbol{x}}_t + (\Delta t)\left[(1 - \gamma)\ddot{\boldsymbol{x}}_t + \gamma\ddot{\boldsymbol{x}}_{t+\Delta t}\right], \tag{20b}$$

where β and γ are constant. Substituting equations (20a) and (20b) into the system equation (19) and solving for $\ddot{\boldsymbol{x}}$ results in

$$K_l \ddot{\boldsymbol{x}}_{t+\Delta t} = F^r_{t+\Delta t}, \tag{21a}$$

$$K_l = \left[K\beta(\Delta t)^2 + C\gamma\Delta t + M\right], \tag{21b}$$

$$F^r_{t+\Delta t} = F_{t+\Delta t} - K\left\{\boldsymbol{x}_t + (\Delta t)\dot{\boldsymbol{x}}_t + (\Delta t)^2(0.5-\beta)\ddot{\boldsymbol{x}}_t\right\} - C\left\{\dot{\boldsymbol{x}}_t + (\Delta t)(1-\gamma)\ddot{\boldsymbol{x}}_t\right\}. \tag{21c}$$

Thus, the accelerations $\ddot{\boldsymbol{x}}_{t+\Delta t}$ can be calculated by solving the matrix equation system (21a). The velocities and displacements can be obtained by means of equations (20a) and (20b). The Newmark method is unconditionally stable provided that $\gamma = 0.5$ and $\beta \geq (2\gamma+1)^2/16$.

2.3. Coupling scheme

Fluid-structure interaction (FSI) is the coupling between the laws of fluid dynamics and those of structural mechanics. Forces exerted on the object lead to deformations depending on the pressure and velocity of the flow and the material properties of the structure. Therefore, the velocity and pressure fields have effects on the structural deformations, and vice versa.

In general, partitioned and monolithic solution procedures have been developed for the numerical simulation of FSI problems [69]. In this paper, as in reference [69] the partitioned method is used which means that separate solvers are chosen: The Cumulant LBM for the fluid solver and the finite element method for the structural solver.

Two possibilities exist to obtain forces on boundaries in LBM calculations: Momentum exchange and Stress integration [70]. Even though the Momentum exchange scheme predicts well integral forces on large structural elements, when it comes to consider the resolution order of the fluid mesh this scheme is not reliable due to the considerable reduction of matching links. Therefore, to evaluate the forces on boundaries with the LBM, here the Pressure/stress integration scheme is chosen. Such scheme benefits from the locally available stress tensor in LBM calculated as

$$S_{IJ} = -c_s^2\rho\delta_{IJ} + \sigma_{IJ} \tag{22}$$

where δ is the Kronecker-Delta. The stresses on the boundary node can be extrapolated from neighboring

cells through the matching squares algorithm [71] by generating isolines on fixed Cartesian grids. In general, there are 16 possibilities of intersection of a structure boundary node and a fluid cell, as discussed in reference [69]. Figure 1 shows two possibilities for the position of the structure inside the fluid domain and the extrapolation of the stresses on the boundary node from neighboring cells. The extrapolation of the stresses for Structure 1 reads

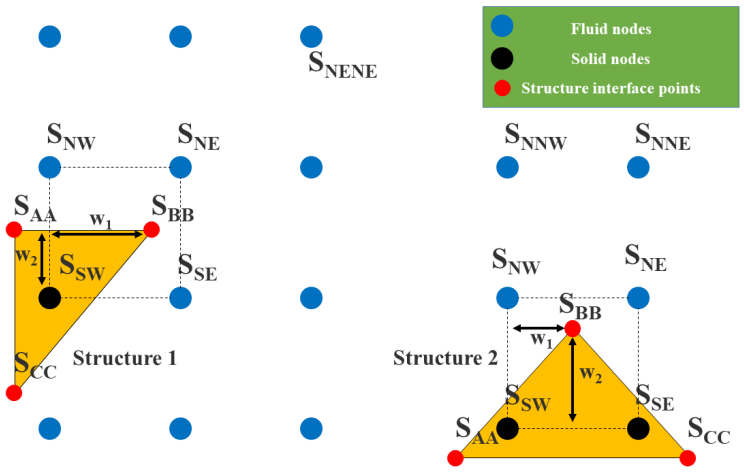

Figure 1: Two possibilities for the position of the structure inside the fluid domain.

$$S_{SW} = 2S_{NE} - S_{NENE}, \tag{23}$$

and the extrapolation for Structure 2,

$$\begin{aligned} S_{SW} &= 2S_{NW} - S_{NMW}, \\ S_{E} &= 2S_{NE} - S_{NNE}. \end{aligned} \tag{24}$$

The next step after extrapolation is a bilinear interpolation for the stresses

$$S = (1 - w_1)(1 - w_2) S_{SW} + w_1 (1 - w_2) S_{SE} + w_1 w_2 S_{NE} + (1 - w_1) w_2 S_{NW} \tag{25}$$

where w_1 and w_2 are normalized weight factors.

By integrating along the boundary Γ the scalar product of the stress tensor times the unit normal vector,

the load vector is calculated,

$$F = \int_{\Gamma} S \cdot n \, \mathrm{d}\Gamma. \tag{26}$$

Considering the fact that the stress components are linear (figure 2), the load vector at point BB using equation 26 equals to

$$F_{BB} = (0.25S_{AA} + 0.75S_{BB})\, n_{AABB} 0.5 l_{AABB} + (0.75S_{BB} + 0.5S_{CC})\, n_{BBCC} 0.5 l_{BBCC}. \tag{27}$$

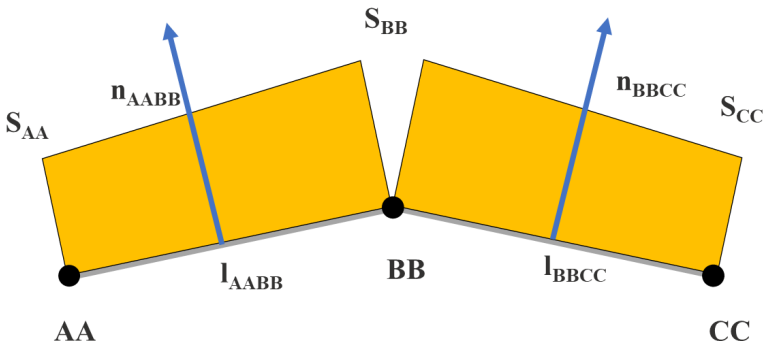

Figure 2: Force calculation from stress.

Owing to the two different grids for structure and fluid, an interface mesh is used to couple both meshes. This mesh is made of a polyline at which physical quantities are required to be stored. The interface mesh can be adapted by the FEM and LBM solvers. Due to the effect of the fluid and the structure on each other there is the possibility that after some structure movement a node in the fluid domain relocates to the solid domain and vice versa. Therefore, the algorithm must activate and deactivate the nodes inside the domains (Fig 3). In addition, the local velocity at the new fluid node is obtained from linear interior extrapolation. The pressure and the higher order moments are calculated based on a local Poisson type of iteration [72]. The distribution functions of the new active node (fluid) are constructed or initialized as the summation of the equilibrium functions, calculated by extrapolating the velocity and the density, plus the non-equilibrium parts, obtained by the previously determined pressure and higher order moments [69, 70, 72].

The FSI algorithm is depicted in Fig 4. The FSI algorithm is depicted in Fig 4: First the fluid solver calculates the load vector on the interface mesh points. Second, the loads are transferred through the

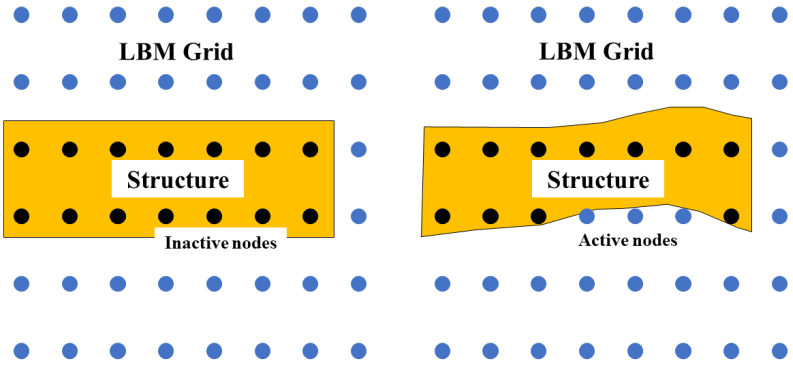

Figure 3: Active (fluid) and inactive (structural) nodes in the LBM grid.

interface mesh. Third, the structural solver calculates the new displacements. Fourth, the new displacements are transferred through the interface mesh. Fifth, the position of the interface surface geometry is calculated by the fluid solver. Sixth, the previous steps are repeated in a sequence.

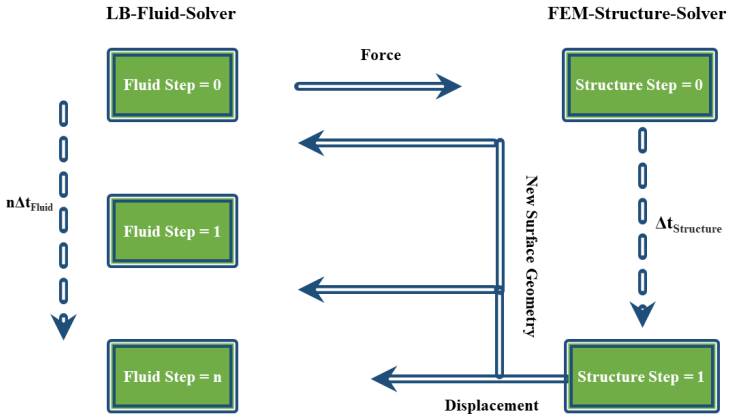

Figure 4: Coupling algorithm.

2.4. The wave equation

Acoustic waves constitute one kind of pressure fluctuations that cause the propagation of energy through a medium: gas, liquid, and solid. Even though there are different ways to obtain the lossy wave equation [73], here it is derived based on references [74, 75].

The general form of the nonlinear Navier-Stokes equation, without external body forces, is

$$\rho\left(\frac{\partial \boldsymbol{u}}{\partial t} + (\boldsymbol{u}.\nabla)\,\boldsymbol{u}\right) = -\nabla p + \left(\frac{4}{3}\eta + \eta_B\right)\nabla\,(\nabla.\boldsymbol{u}) - \eta\nabla\times\nabla\times\boldsymbol{u}, \tag{28}$$

where η is the coefficient of shear viscosity, η_B is the coefficient of bulk viscosity, and $\eta\nabla\times\nabla\times\boldsymbol{u}$ is the dissipation of acoustic energy, which has few effects on linear acoustics.

In general, a quantity called condensation is defined in linear acoustics, $s = (\rho - \rho_0)/\rho_0$ which is the ratio between the deviation from the equilibrium density and the equilibrium density itself, and must be small. In addition, the total pressure equation is written as $p = p_0 + p'$ where p_0 is the atmospheric pressure and p' is the acoustic pressure.

Using the linearized form of equation (28) and the linearized continuity equation $\nabla\cdot\boldsymbol{u} = -\partial s/\partial t$, plus the equation of state $p' = \rho_0 \varsigma_s^2 s$, leads to a lossy wave equation,

$$\left(1 + \tau_s\frac{\partial}{\partial t}\right)\nabla^2 p' = \frac{1}{\varsigma_s^2}\frac{\partial^2 p'}{\partial t^2} \tag{29}$$

where

$$\tau_s = \frac{1}{\rho_0\varsigma_s^2}\left(\frac{4}{3}\eta + \eta_B\right).$$

3. Results and Discussion

In this section, the Cumulant LBM is used first to calculate acoustic dissipation and dispersion for benchmark cases, and the results are compared with theoretical values. Second, spherical wave propagation at a very low viscosity is studied by means of different LB methods and the results are compared with the theoretical solution. Finally, the Cumulant LBM is coupled with a finite element method to study the effect on the flow and sound propagation around one single and two twin cylinders due to SPCH at high Re numbers, as a real engineering FSI case of study.

3.1. Acoustic properties of the Cumulant Lattice Boltzmann Method

The LBM has been used to model the aerodynamic and hydrodynamic characteristics of different phenomena, moreover, it has the capability to directly obtain the acoustic field without additional computational cost. In this section, the aim is to study the accuracy of the Cumulant LBM in predicting acoustic properties for benchmark cases before extending it to fluid-structure interaction applications in the following sections. Initially, the dispersion and dissipation relations of the propagation of a plane wave are presented based on

the temporal and spatial analyses from equation (29) as in Bres et al.'s work [33]. Then, the propagation of a standing plane wave and a planar acoustic pulse of Gaussian shape is implemented using the Cumulant LBM. Numerical errors, finally, for the dissipation and dispersion parameters are computed for these cases.

3.1.1. Planar standing wave

A standing plane acoustic wave is considered for a temporal analysis as a first configuration. The calculated dissipation and dispersion relations based on the temporal analysis of equation (29) [33] lead to

$$c_T = \varsigma_s \sqrt{1 - \left(\frac{k\nu}{\varsigma_s}\right)^2}, \tag{30a}$$

$$\alpha_T = k^2 \nu, \tag{30b}$$

where k is the wave-number. The assumptions for this set-up are listed in table 1. For a linear acoustic problem, the perturbation amplitude p' is chosen small compared to the average pressure p_0. Periodic boundary conditions are applied in both directions. The time step is chosen so that we have dispersion and dissipation effects, but not boundary side effects.

Table 1: Parameters for the planar standing wave

Variables	$p'(x,y,0)$	ρ'	u'	v'	A
Description	$A\sin\left(\frac{2\pi x}{\lambda}\right)$	$\frac{p'}{\varsigma_s^2}$	$\frac{p'}{\rho_0 \varsigma_s}$	0	$10^{-3} p_0$

The acoustic pressure at time t is [33]

$$p'(x,y,t) = A \exp\left[-\left(\alpha_T + \alpha_T^{num}\right) t\right] \sin\left[k\left(x - \left(c_T + c_T^{num}\right) t\right)\right], \tag{31}$$

where the superscript "*num*" denotes the deviation between the numerical and theoretical values. Therefore, c_T^{num} and α_T^{num} are the deviation phase speed and temporal dissipation rate, respectively. These coefficients can be derived, for any location, from the plot of the perturbation versus time using nonlinear least-squares fitting and equations (30a) and (30b). In addition, the results can be presented either as a function of the number of the points per wavelength $N_{ppw} = \lambda/\Delta x$ or the non dimensional wave-number $k\Delta x = 2\pi/N_{ppw}$.

To study the accuracy of the propagation of waves using the Cumulant LBM, various viscosities and different resolutions (i.e. number of points per wavelength) are considered. One of the most important properties for characterizing fluid flow which has a vital effect on the accuracy of acoustics simulations is

the bulk viscosity [58, 27, 64]. Figure 5 shows the comparison between numerical results for two different choices of the bulk viscosity against the analytical solution. The subfigures show the results for values $\nu = 1.5 \times 10^{-3}\mathrm{m}^2/\mathrm{s}$ and $\nu = 1.5 \times 10^{-1}\mathrm{m}^2/\mathrm{s}$ of the kinematic viscosity and $N_{ppw} = 18$ point per wavelength. Case 1: the relaxation time for the bulk viscosity is chosen based on equation (8). Case 2: the value of the relaxation time for the bulk viscosity is chosen as 1. Therefore, a wrong selection of the bulk viscosity leads to inaccurate results.

Figure 6 presents the acoustic pressure time-history for $\nu = 1.5 \times 10^{-2}\mathrm{m}^2/\mathrm{s}$ with $N_{ppw} = 12$ points per wavelength. The relative numerical error of the phase speed and temporal dissipation rate are presented as functions of the non dimensional wave-number in table 2. The table shows that the deviations from the theoretical values are small, even for a relatively low resolution with 12 points per wavelength: about 0.77 percent in the phase speed and 0.018 percent in the dissipation rate. It should be noted that by reducing the viscosity, the phase speed and dissipation errors are almost constant. Thus the results are only a function of N_{ppw} and are independent of viscosity in the range of interest. It can be concluded that the results of the Cumulant LBM show a good agreement with the theoretical values and behave similarly to the numerical values of reference [33].

Table 2: Relative numerical error of the specified acoustic properties as a function of the non-dimensional wave-number ($k\Delta x$) for the planar standing wave.

$k\Delta x$	$\pi/12$	$\pi/6$	$\pi/4$	$\pi/3$	$\pi/2$
c_T^{num}/c_T	-1.8×10^{-3}	-7.7×10^{-3}	-1.7×10^{-2}	-3.1×10^{-2}	-7.2×10^{-2}
α_T^{num}/α_T	-7.5×10^{-4}	-1.8×10^{-4}	-1.2×10^{-3}	-4.3×10^{-3}	-2.5×10^{-2}

3.1.2. Planar pulse wave

A planar pulse wave is studied for a spatial analysis where acoustic waves of fixed frequencies propagate through the domain. The dissipation and dispersion relations derived, based on the spatial analysis from equation (29) [33] are

$$c_S = \sqrt{2}\varsigma_s \sqrt{\frac{1 + (\omega\tau_s)^2}{\sqrt{1 + (\omega\tau_s)^2} + 1}}, \tag{32a}$$

$$\alpha_S = \frac{\omega}{\sqrt{2}\varsigma_s} \sqrt{\frac{\sqrt{1 + (\omega\tau_s)^2} - 1}{1 + (\omega\tau_s)^2}}. \tag{32b}$$

With the assumptions presented in table 3, a planar pulse of Gaussian shape initially propagates from

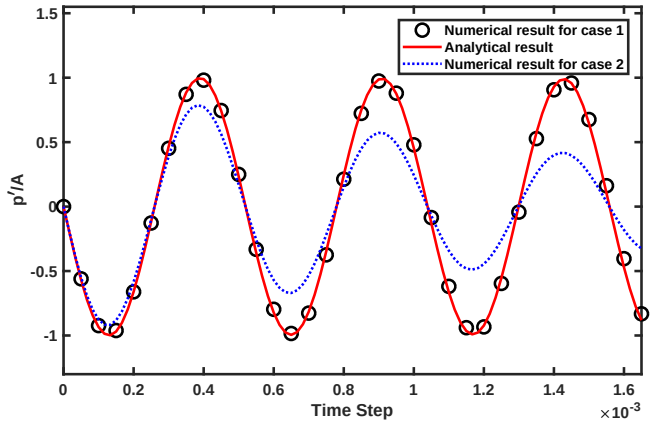

(a) $\nu = 1.5 \times 10^{-3} \mathrm{m}^2/\mathrm{s}$.

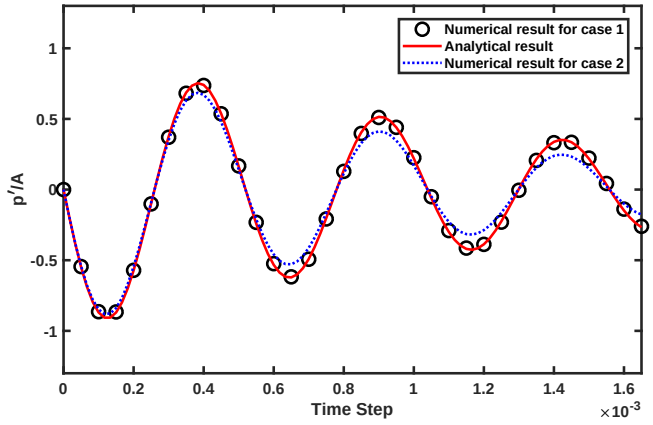

(b) $\nu = 1.5 \times 10^{-1} \mathrm{m}^2/\mathrm{s}$.

Figure 5: Non-dimensional acoustic pressure p'/A vs. time history [s] at (0,0) for the planar standing wave considering two different choices for the bulk viscosity: Case 1 where the relaxation time for the bulk viscosity is chosen based on equation (8)) and Case 2 where the value of the relaxation time for the bulk viscosity is chosen as 1.

the origin through the domain where periodic boundary conditions are imposed. The time step is chosen in a way that the pulse passes without interfering with the boundaries.

Table 3: Parameters for the planar pulse wave

Variables	$p'(x,y,0)$	ρ'	u'	v'	A	σ
Description	$A\exp\left(-\ln(2)\frac{x^2}{\sigma^2}\right)$	$\frac{p'}{\varsigma_s^2}$	$\frac{p'}{\rho_0 \varsigma_s}$	0	$10^{-3}p_0$	0.03

The Fourier transform of the pressure time history of the passing wave gives the Fourier coefficient of

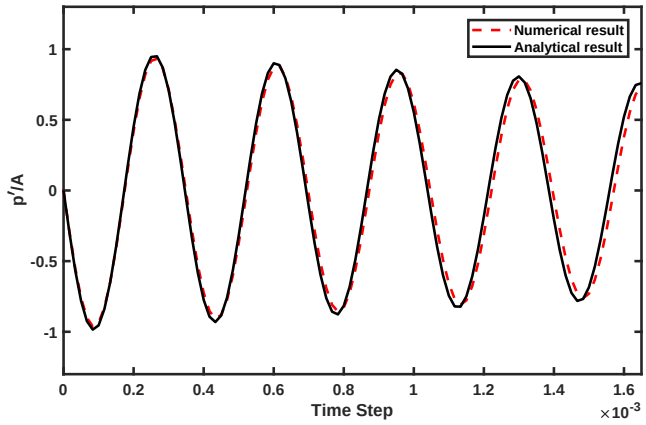

Figure 6: Non-dimensional acoustic pressure p'/A vs. time history [s] at (0,0) for the planar standing wave.

pressure $\widehat{p'}(x,\omega)$

$$\widehat{p'}(x,\omega) = \widehat{p'}(x,0)\exp\left[-\left(\alpha_S + \alpha_S^{num}\right)x\right]\exp\left[i\omega\frac{x}{c_S + c_S^{num}}\right] \tag{33}$$

which is similar to the solution of equation (29) [33], where c_S^{num} and α_S^{num} are the deviation phase speed and spatial dissipation rate, respectively. The coefficients are calculated as a function of the frequency using the phase and amplitude of the ratio $\widehat{p'}(x,\omega)/\widehat{p'}(x,0)$ and the dissipation and dispersion relations given in equations (32a) and (32b).

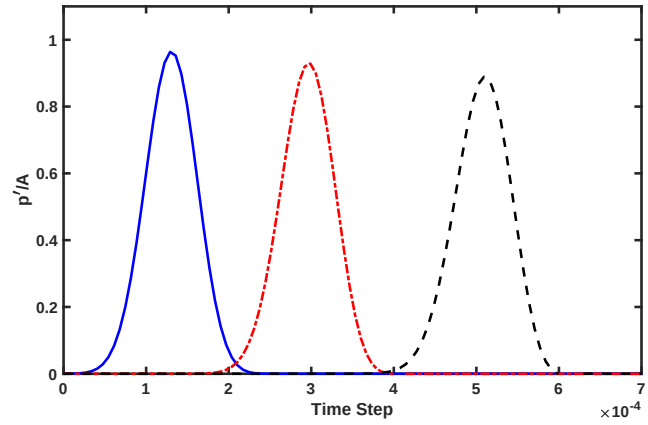

Figure 7: Non-dimensional acoustic pressure p'/A vs. time history [s] at origin (————), 0.056m (–· –· –) and 0.128m (– – – – –) from the reference position, for the planar pulse wave.

Figure 7 presents the acoustic pressure time-history of the propagation of the planar Gaussian pulse for $\nu = 2.36\times10^{-2}\mathrm{m}^2/\mathrm{s}$ with a resolution $\Delta x = 0.004\mathrm{m}$. It shows the planar wave as it moves toward the positions

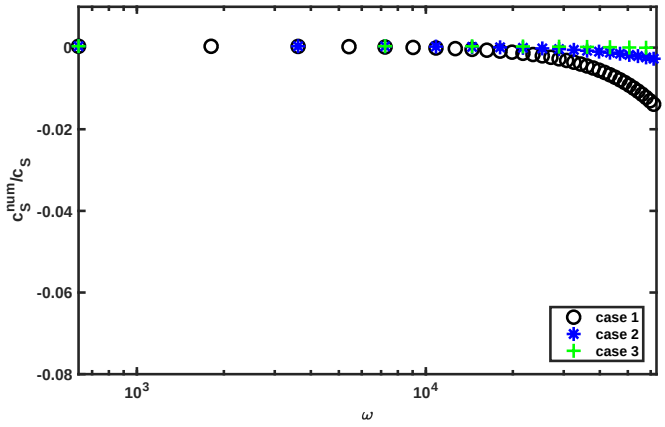

(a) Phase speed.

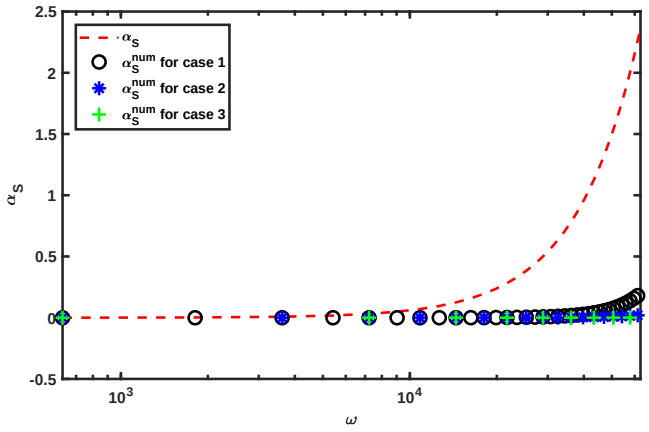

(b) Dissipation rate [Np/m].

Figure 8: Numerical error of the specified acoustic properties for the planar pulse wave as functions of the angular frequency [Hz] ($\nu = 2.36 \times 10^{-2}\text{m}^2/\text{s}$ and different resolution).

0.056m and 0.128m from the reference position. In addition, the amplitude of the wave changes with the propagation distance from the reference point. The relative numerical error of the phase speed c_S^{num}/c_S and the dissipation rate α_S^{num} (in Np/m, where Np is a dimensionless unit called neper) are depicted in figures 8a and 8b as functions of the angular frequency, for resolutions $\Delta x = 0.004$m (Case 1), $\Delta x = 0.002$m (Case 2), and $\Delta x = 0.001$m (Case 3). Errors are small as in the planar standing wave example, even for the relatively low resolution $\Delta x = 0.004$m. Various viscosities, as in the first set-up, are used to study the predictive accuracy of the Cumulant LBM in a traveling planar pulse. Figure 9 presents the relative numerical error of the dissipation rates for $\nu = 2.35 \times 10^{-4}\text{m}^2/\text{s}$ and resolution $\Delta x = 0.004$m. It shows the same behavior as in the planar standing wave case regarding the reduction of viscosity. To conclude, the results of the Cumulant LBM show a good agreement with the theoretical values for the dissipation rate.

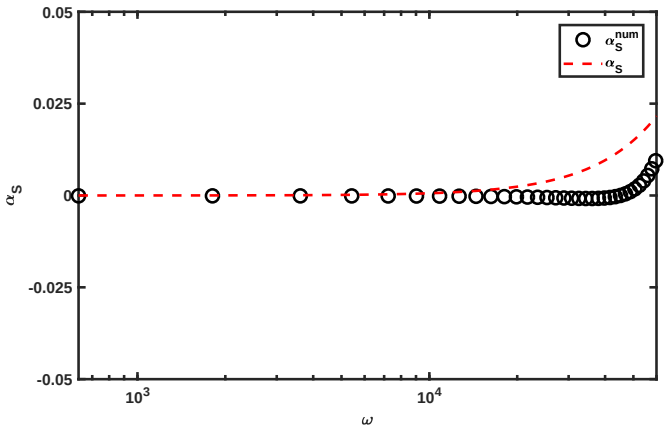

Figure 9: Numerical error of the dissipation rate [Np/m] for the planar pulse wave as a function of angular frequency [Hz] (for $\nu = 2.35 \times 10^{-4}\mathrm{m}^2/\mathrm{s}$ and resolution $\Delta x = 0.004\mathrm{m}$).

3.2. Spherical wave

Unlike section 3.1 where the wave propagates in a straight line, in most real cases, sources generate a wave which expands in a set of spherical wave fronts. The analytic solution for an outgoing cylindrical wave obtained from equation (29) in cylindrical coordinates is

$$\rho'(x, y, t) = A H_0^{(2)}(kr) \exp(i\omega t), \tag{34}$$

where $H_0^{(2)}$ is the zeroth-order Hankel function of the second kind [75]. In the following section, spherical wave propagation is studied using the Cumulant LBM for a low value of the viscosity $\nu = 1.5 \times 10^{-5}\mathrm{m}^2/\mathrm{s}$.

3.2.1. Acoustic pulse

A pseudo-2D acoustic pulse is investigated as a first configuration of spherical wave propagation, where the pulse assumes a Gaussian shape. This is the most standard aeroacoustic 2D benchmark case [76]. Table 4 shows the assumptions of this setup. Periodic boundary conditions are chosen. However, the time step as well as the total simulation time are set to avoid any boundary effects.

For very low viscosities and small amplitudes of the acoustic perturbation, equation (34) results in the density fluctuation $\rho'(x, y, t)$ [77]:

$$\rho'(x, y, t) = \frac{A}{2\alpha} \int_0^\infty \exp\left(\frac{-s^2}{4\alpha}\right) \cos(\varsigma_s t s)\, J_0(rs)\, s\, \mathrm{d}s, \tag{35}$$

where J_0 is the zeroth-order Bessel function of the first kind.

In this set-up, an acoustic pulse is generated by an initial Gaussian pressure distribution from the center of the computational domain, then the wave front of the pulse expands rapidly throughout the domain.

Table 4: Parameters for the pseudo-2D acoustic pulse

Variables	ρ'	u'	v'	ϵ	α	b	r
Description	$\epsilon \exp\left(-\alpha r^2\right)$	0	0	10^{-3}	$\frac{\ln(2)}{b^2}$	10^{-1}	$\sqrt{x^2+y^2}$

Figure 10 draws a comparison between the numerical and analytical solutions for the density function of the acoustic pulse propagation. There is a good agreement between the Cumulant LBM and the analytical solution at time steps 10 (figure 10a) and 100 (figure 10b). The results show that the Cumulant LBM faithfully reproduces the spherical acoustic pulse wave at a very low viscosity.

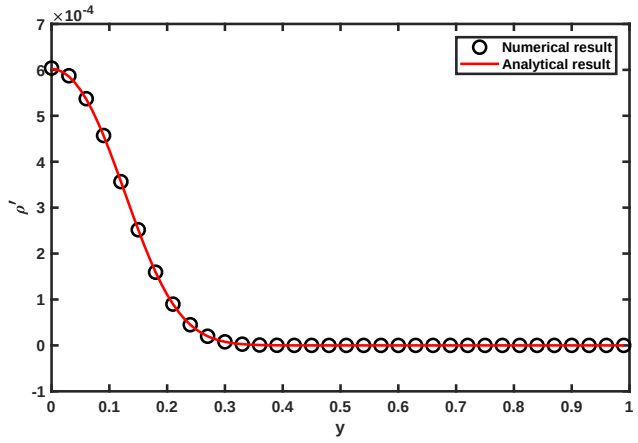

(a) Time step=10.

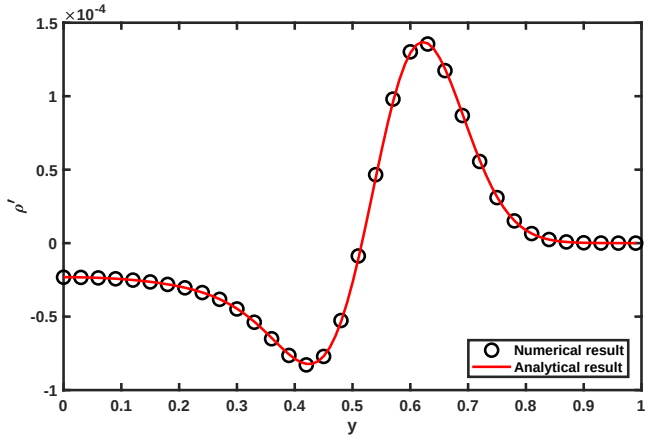

(b) Time step=100.

Figure 10: The comparison of the analytical and numerical values of the perturbation ρ'[kg/m^3].

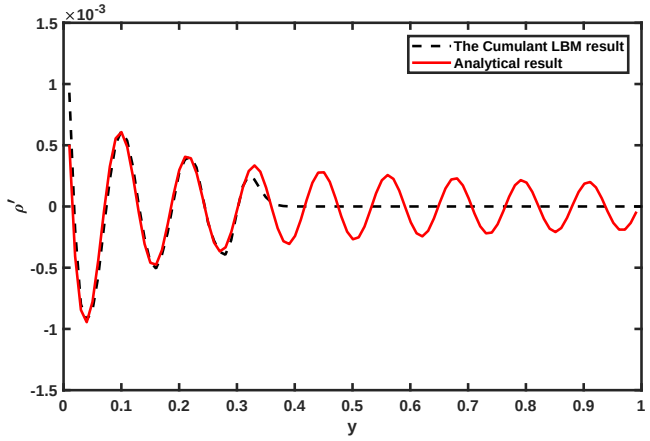

(a) Time step 60.

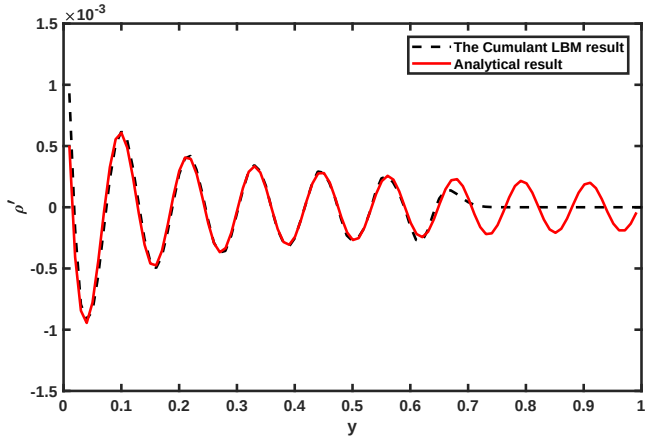

(b) Time step 120.

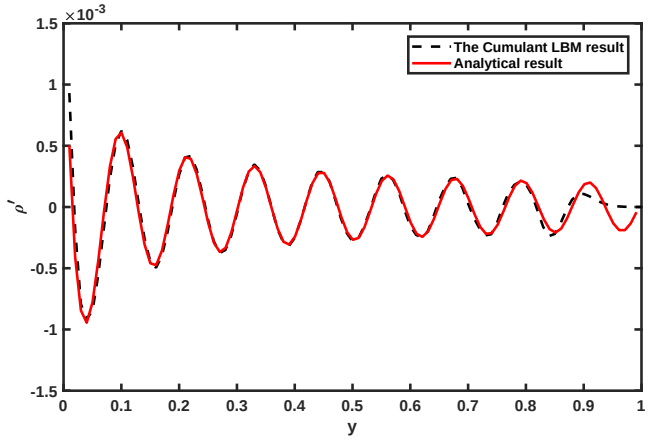

(c) Time step 160.

Figure 11: Comparison of the stationary analytical and numerical values of the perturbation ρ' [kg/m^3] for the Cumulant LBM.

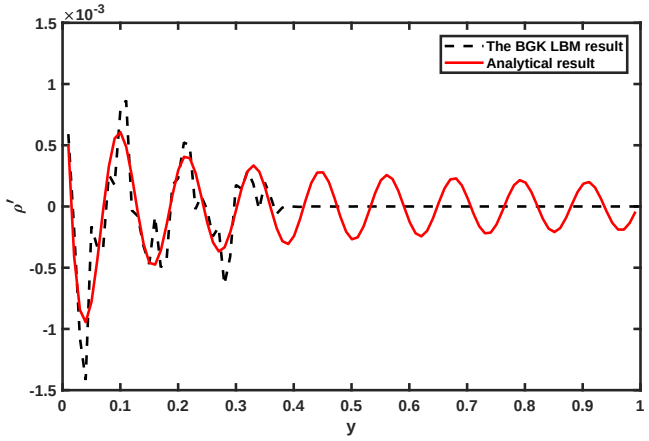

(a) Time step 60.

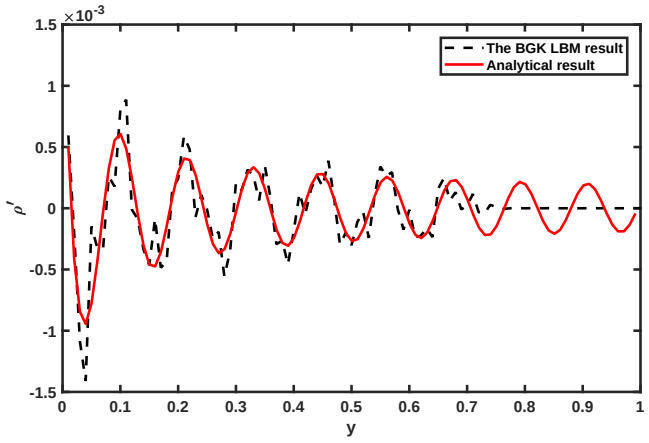

(b) Time step 120.

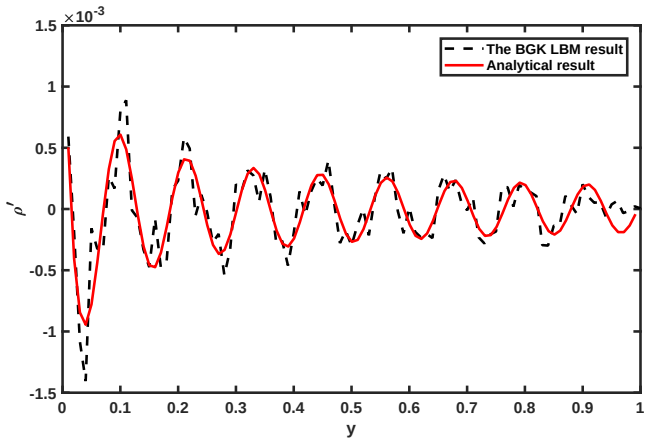

(c) Time step 160.

Figure 12: Comparison of the analytical and numerical values of the perturbation ρ' [kg/m^3] for the BGK LBM.

3.2.2. Acoustic point source

In the preceding section, finite acoustic waves propagate throughout the domain from an initial wave distribution. It is time to study infinite waves such as those produced by a point source which emits a

sinusoidal signal. The assumptions for this set-up are presented in table 5.

Table 5: Parameters for the acoustic point source

Variables	ρ'	ω	B	r	T
Description	$B\sin(\omega t)$	$\frac{2\pi}{T}$	10^{-2}	$\sqrt{x^2+y^2}$	20

To simulate this point source, a sinusoidal density function is fixed to the LBM lattice located in the center of the domain as in references [78] and [75]. Furthermore, the velocity can be chosen as a constant ($u = 0$) or based on the particles streaming into the source node to guarantee conservation inside the domain. In addition, periodic boundary conditions are imposed.

In order to make a meaningful assessment of the results of different LB methods regarding the stationary analytic solution for the point source cylindrical waves given by equation (34), we used the same method as Viggen [75] and Sagaut et al. [79]. Figures 11 and 12 show the comparison between the numerical result and the stationary analytical solution for the propagation of the density function of the acoustic point source wave. The comparison shows a good match between the Cumulant LBM result and the stationary analytical solution at time steps 60 (figure 11a), 120 (figure 11b), and 160 (figure 11c). It should be noted that the reason why the numerical density is 0 beyond a certain point is that the spherical waves spreading from the source have not yet reached those points at that time. The plots for different time steps show that the unsteady spherical waves follow the stationary analytical solution by overlapping it over time. In addition, as Viggen [75] and Sagaut et al. [79] have shown, the stationary analytical graph can give a mature and understandable prediction of the wave motion throughout the whole domain. On the contrary, the comparison does not draw a good match between the BGK LBM and the analytical solution at time steps 60 (figure 12a), 120 (figure 12b), and 160 (figure 12c). Even though, the numerical results follow the analytic solution, they display noisy behavior, as the method is unstable at low viscosities. In a nutshell, the acoustic point source example can illustrate the power of the Cumulant Lattice Boltzmann method to naturally simulate acoustic behavior even at a very low viscosity.

3.3. Splitter plates attached to a cylinder looking like hair (SPCH)

There is a growing need for the SPCH to control flow and Aeolian tones in many industries. Aeolian tones, i.e. sound generated by flow over objects, is relevant to airframes at high Reynolds numbers. To have a good assessment of such devices, the finite element method as a structural solver is coupled with the Cumulant LBM as a fluid solver. Thus, this section will challenge the Cumulant LBM in a real engineering

FSI modeling problem, by focusing on the influence of the SPCH on the dynamics of a cylinder wake flow.

Six cases are examined in this section, presented in table 6 and figure 13. These cases consist of a single cylinder and two twin cylinders aligned perpendicularly to the free stream and whose centers are 3 diameters apart. The origin of coordinates is the mid-point between the two cylinder centers. Case 1 and Case 4 should be considered as references for Cases 2 and 3, and Cases 5 and 6, respectively, when describing figures 14, 17, and 18. Table 7 shows the assumptions for the fluid and the domain in these setups. The Reynolds number is chosen based on the cylinder diameter and the free stream velocity. The fluid characteristics are set based on air. The flexible flaps are distributed homogeneously along the aft part of the segments facing the downstream direction at 60 degrees from the center. In addition, the Young modulus is $12.525 \times 10^6 \mathrm{kg/ms^2}$ and the structural density is $\rho_{solid} = 1000 \mathrm{kg/m^3}$. The boundary conditions include velocity inlet (U_0), non-reflecting [64] and pressure outlet boundary conditions, plus the bounce back scheme [69]. It should be noted that we used the modified bounce back scheme developed in [80, 81] for the velocity, which is second order accurate for arbitrarily shaped boundaries.

Table 6: Cases studied for the SPCH

Cases	Figures	Cylinders	Flaps	Length of flaps	Width of flaps	State of flaps
1	13a	1	0	×	×	×
2	13c	1	3	r	$0.001\,m$	Stationary
3	13e	1	2	$2r$	$0.001\,m$	Moving
4	13b	2	0	×	×	×
5	13d	2	3	r	$0.001\,m$	Stationary
6	13f	2	2	$2r$	$0.001\,m$	Moving

where r is the radius of the cylinder.

To validate the results, the Cumulant LBM results for Cases 1 and 4 are compared with experimental and several previous numerical studies.

Table 7: Parameters for the SPCH study

Variables	U_∞	D	fluid	Domain length	Domain width
Values	$24.5\,m/s$ & $73.5\,m/s$	$0.00955\,m$	air	$60\,D$	$30\,D$

Table 8 presents the comparison between experimental [82, 83] and Cumulant LBM results on the Strouhal number, a dimensionless number describing oscillating flow mechanisms. It is defined as St =

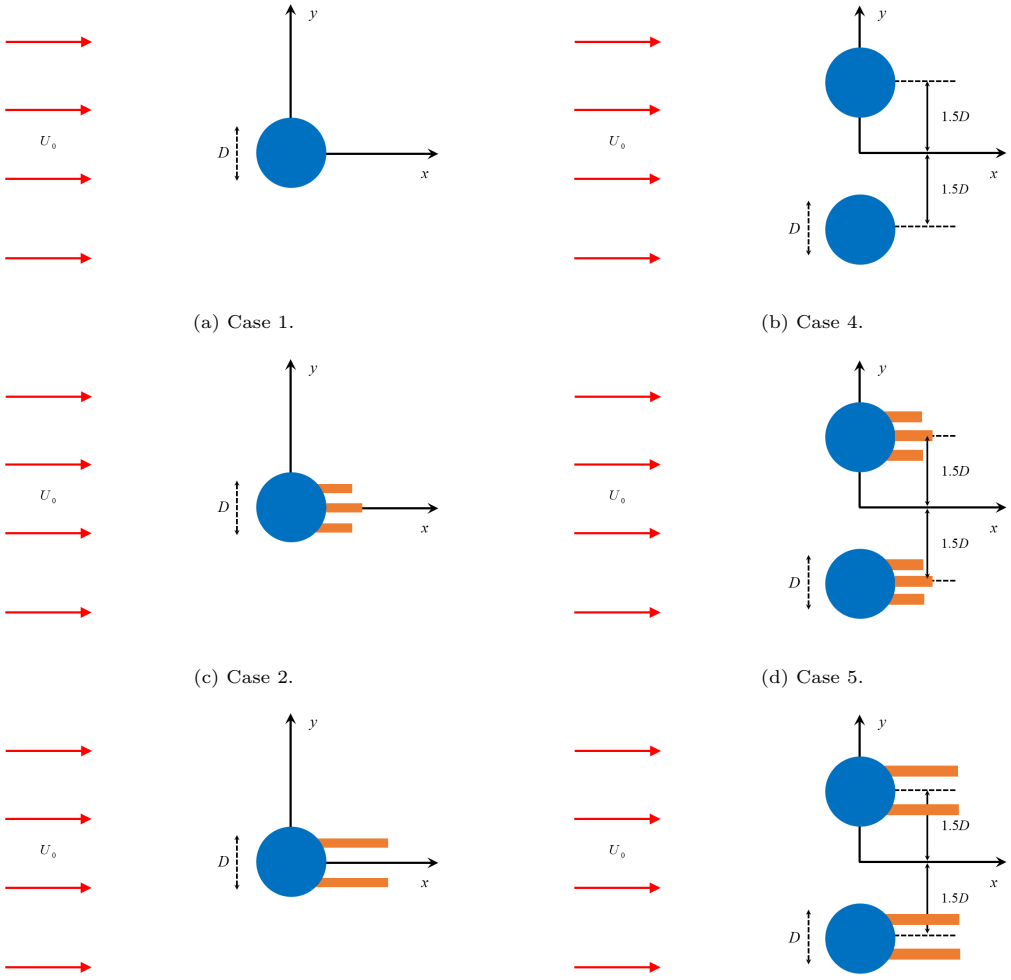

(a) Case 1.

(b) Case 4.

(c) Case 2.

(d) Case 5.

(e) Case 3.

(f) Case 6.

Figure 13: Computational domain of the cases studied for the SPCH problem.

$2r/(U_\infty T) = (2rf)/U_\infty$, where T and f are the period and the frequency of the vortex shedding, respectively. The results in table 8 are for Case 1 of figure 13 at $Re = 1.58 \times 10^4$. The results are presented for three grid resolutions. The Strouhal number for grid resolutions 2 and 3 shows less than 1 percent deviation from the reference data.

Table 9 shows a similar comparison for Case 4 and $Re = 1.58 \times 10^4$. It shows that the results for grid resolutions 2 and 3 are between the results of Guenanff and Lockard [84]. Therefore, to reduce the computational cost, the grid resolution 2 is used.

The generation of vorticity past the cylinders under consideration can give a good estimation of the effects of SPCH. Figure 14 shows the spread of the vorticity in the wake past the cylinder for Cases 1-3 and

Table 8: The Strouhal number for Case 1

	St
Experimental result [82, 83]	0.201
Cumulant LBM result for grid resolution 1 (nodes=525056)	0.185 ± 0.001
Cumulant LBM result for grid resolution 2 (nodes=1050112)	0.203 ± 0.005
Cumulant LBM result for grid resolution 3 (nodes=2100225)	0.202 ± 0.011

Table 9: The Strouhal number for Case 4

	St
Kia et al. [85]	0.205
Cheong et al. [86]	0.204
Guénanff et al [84]	0.212
Lockard [84]	0.222
Loh et al. [84]	0.239
Cumulant LBM result for grid resolution 1 (nodes=525056)	0.194 ± 0.001
Cumulant LBM result for grid resolution 2 (nodes=1050112)	0.218 ± 0.004
Cumulant LBM result for grid resolution 3 (nodes=2100225)	0.215 ± 0.009

$Re = 4.7 \times 10^4$. Figure 14a shows a wavy layer of discrete vorticity moving downstream in the wake of the cylinder for Case 1. Near the cylinder the wave pattern is sharper than in the far downstream, because of transport of momentum within the system caused by random and chaotic time dependent motion occurring in the region. In addition, the figure shows that the spatial formation of vorticity is asymmetrical. The position of the vortices changes in time; in fact, the vorticity oscillates and radiates sound waves into the flow. Figure 14b depicts the spread of vorticity created by three flaps which are not allowed to move. It shows that the use of a sparse set of such flaps can passively manipulate the vortex shedding generated in the wake of bluff bodies. The transverse distance of the vorticity from the center-line reduces. Figure 14c depicts the spread of the vorticity caused by two flaps with length $L = 2r$ allowed to move. The mobility of flaps is one of the major elements having great effects on the vorticity. It is clear that the presence of flaps alters the phase within the vortex shedding cycle such that the transversal dislocation of the shed vorticity is reduced. Accordingly, the vorticity is not arranged in the same manner as in Case 1, instead it is shed in a row along the center-line. Figure 15 illustrates the flap displacement vs. time for Case 3. The black and red lines show the upper and lower flaps. In addition, the '*' symbols indicate the times chosen to depict the states of the flaps in figure 16.

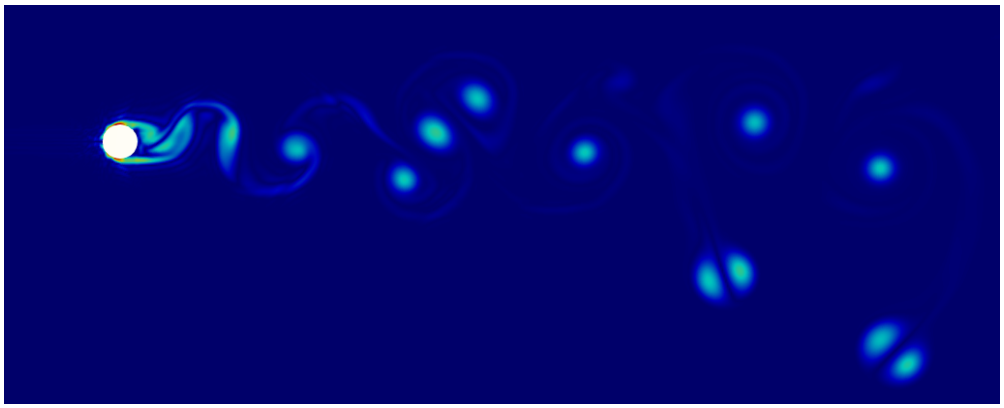

(a) Case 1.

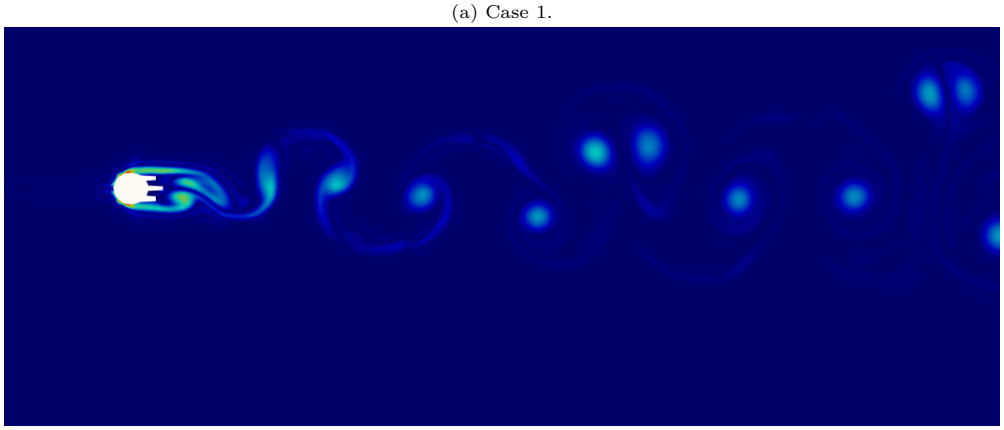

(b) Case 2.

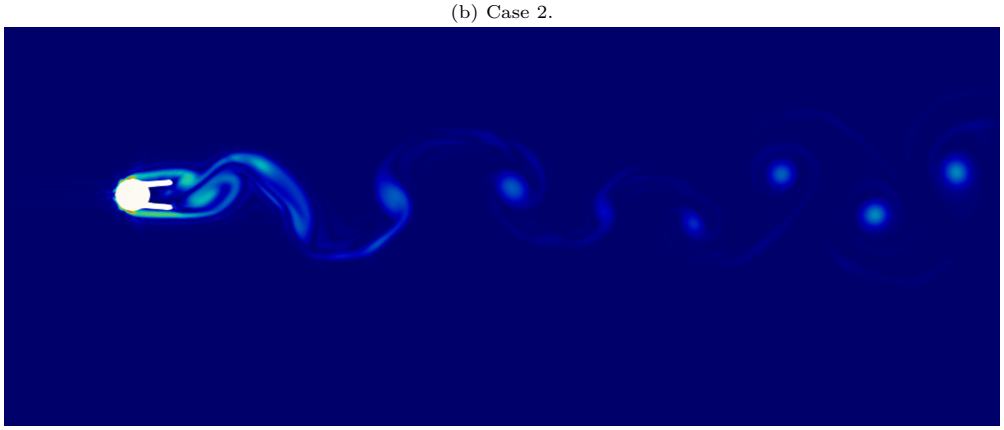

(c) Case 3.

Figure 14: Spread of the vorticity [$1/\Delta t$] in the wake behind a cylinder for Cases 1-3.

Figure 17 illustrates the spread of the vorticity in the street behind two twin cylinders (Cases 4-6) and $Re = 4.7 \times 10^4$. In Figure 17a, the contour plots show that the noise source for Case 4 is of dipolar nature. Far from the twin cylinders, however, the pattern of the vorticity changes. The use of three flaps limits their

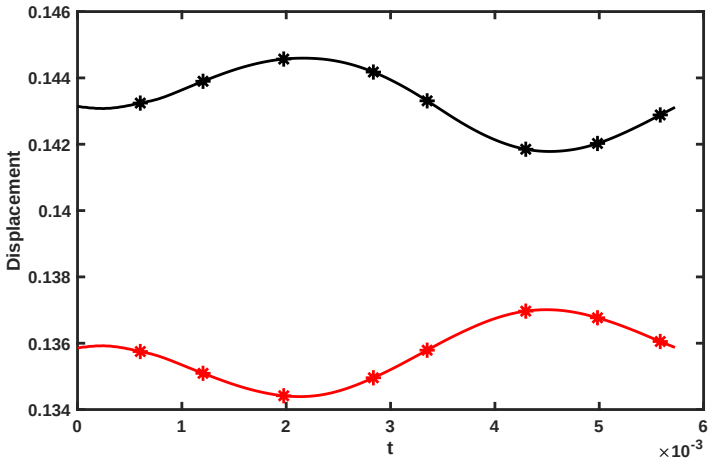

Figure 15: Displacement [m] vs. time [s]

motion. The size and location of the vorticity change, especially when moving away from the twin cylinders as depicted in Figure 17b. By using the length $L = 2r$ for flaps and letting them fluctuate as in Case 6, the arrangement of the vorticity in the wake changes considerably. Figure 17c demonstrates that the vorticity is broken into smaller pieces and its strength reduces. Therefore, there is a significant effect of such moving flaps on the flow over twin cylinders.

The point located at $(0D, 0.63D)$ from the center of the single cylinder (or the upper cylinder in the twin-cylinder configurations) is selected for recording data to depict the sound pressure level (SPL), where D is the cylinder diameter. Figure 18 shows the SPL vs. frequency, computed by Fast Fourier transform, for $Re = 4.7 \times 10^4$. The SPL in dB is relative to the level of 20mPa. The figure shows that the cylinder without flaps has higher frequency, however, its SPL is lower than cylinders with 3 flaps. In addition, it shows that for twin cylinders, $L = 2r$ and moving flaps, the frequency and the SPL reduce. It means that flaps with special characteristics can modify the shedding cycle past the cylinder, having an effect on the generated sound, and can reduce the wake deficit. Young's modulus has a great effect on the flexibility and the mobility of the flaps, resulting in changes in sound and flow patterns. Figure 19 shows the SPL vs. frequency for one cylinder with two flaps of length $3r$ for two different Young's modulus ($E_1 = 36.21 \times 10^6 \text{kg/ms}^2$, $E_2 = 36.23 \times 10^6 \text{kg/ms}^2$) and $Re = 4.7 \times 10^4$. It should be noted that the Young's modulus is chosen to let flaps move but not touch each other. The less the Young's modulus, the higher the SPL and the frequency.

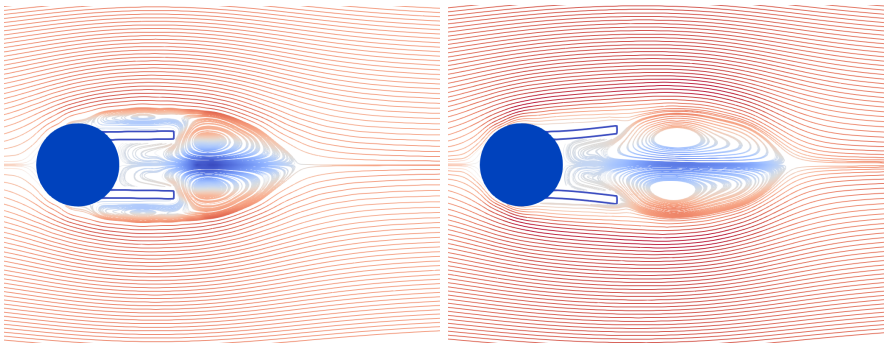

(a) Time 0.006 s.

(b) Time 0.0012 s.

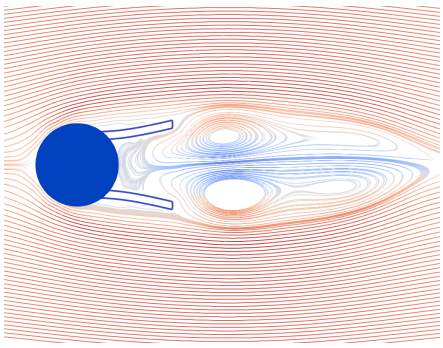

(c) Time 0.002 s.

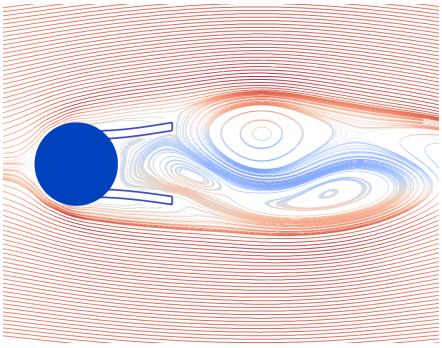

(d) Time 0.0028 s.

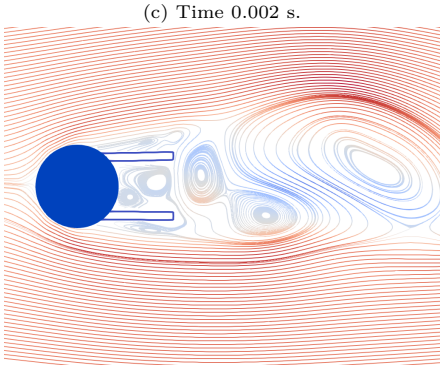

(e) Time 0.0034 s.

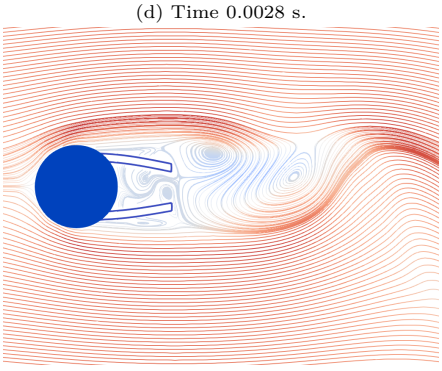

(f) Time 0.0043 s.

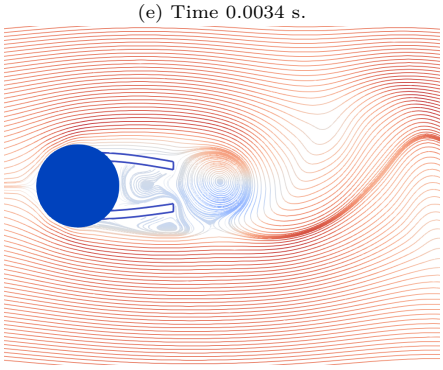

(g) Time 0.005 s.

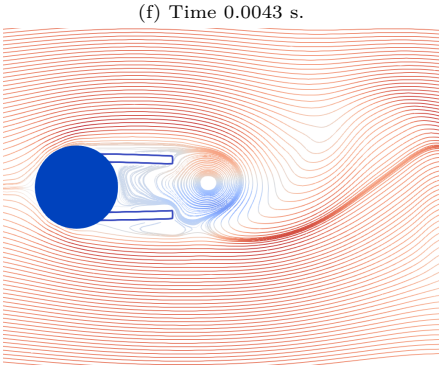

(h) Time 0.0056 s.

Figure 16: State of the flaps for eight selected times.

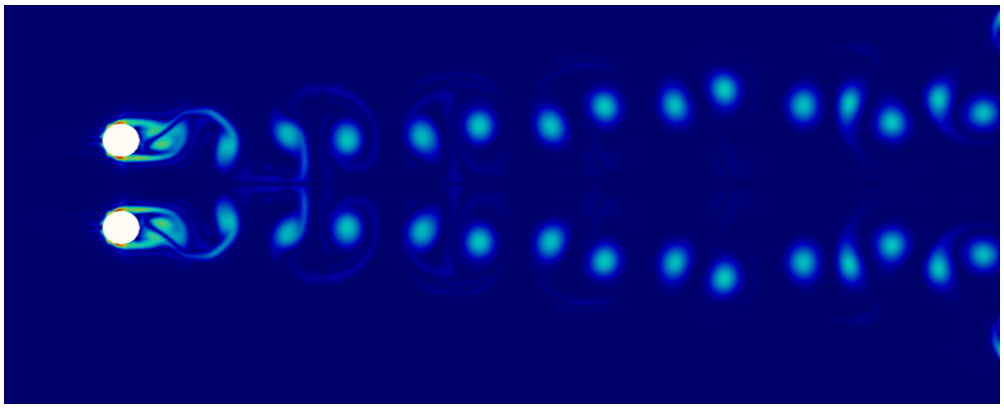

(a) Case 4.

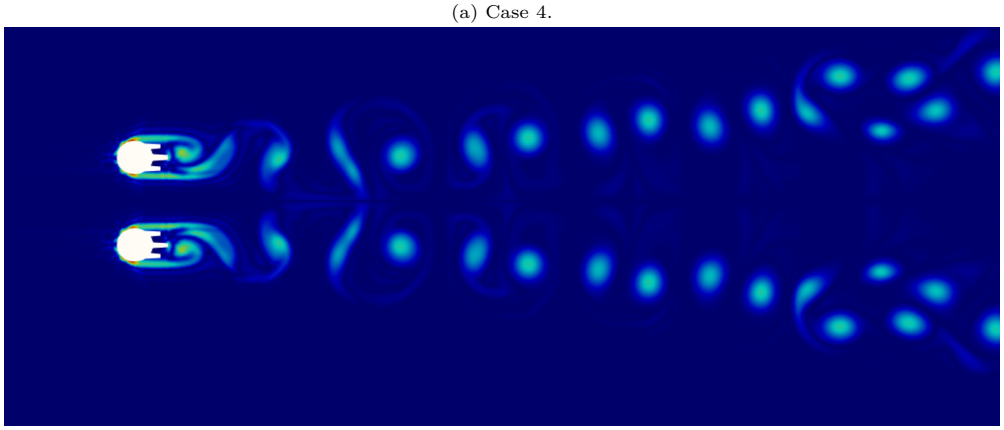

(b) Case 5.

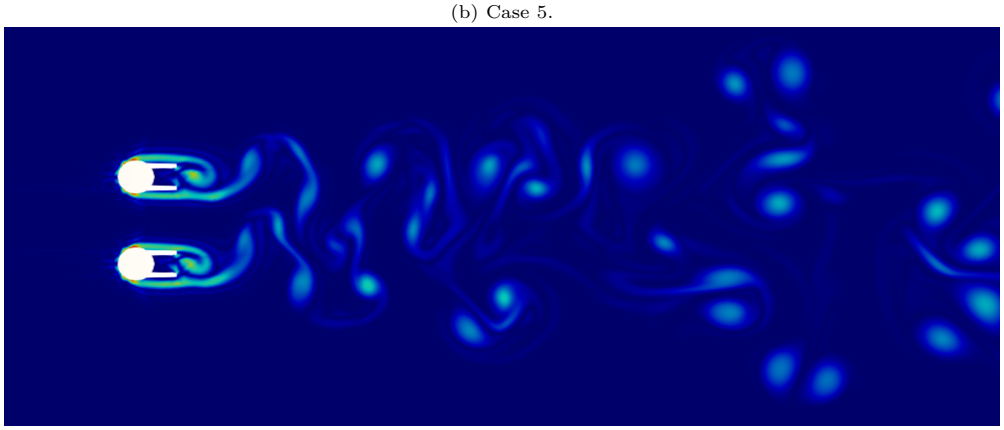

(c) Case 6.

Figure 17: Spread of the vorticity [$1/\Delta t$] in the wake behind twin cylinders for Cases 4-6.

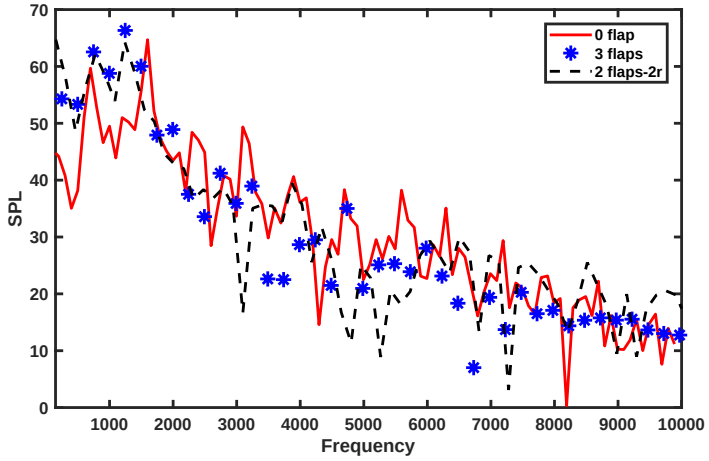

(a) Single cylinder cases.

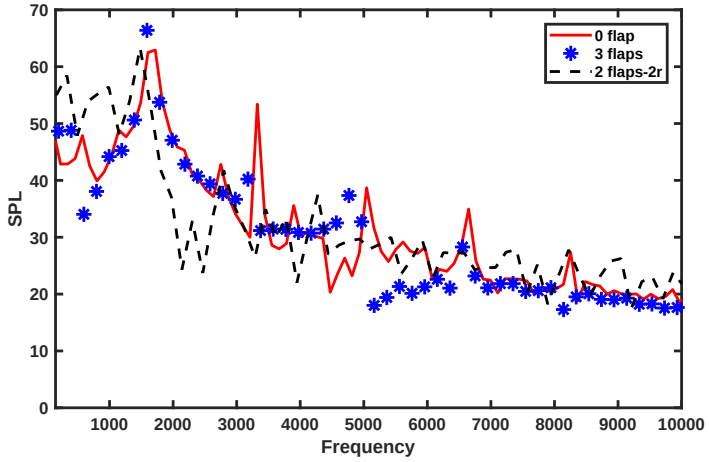

(b) Twin cylinder cases.

Figure 18: Sound pressure level [dB] as a function of frequency [Hz].

4. Conclusion

In this paper a theoretical and numerical study of different types of sound wave propagation, their dissipation and dispersion rates, was carried out using the Cumulant LBM. In addition, the Cumulant LBM was coupled to a finite element method creating a FSI platform to model the effects of simpler splitter plates attached to the cylinder which look like hair on the flow and sound pattern in cylinder wakes.

The temporal and spatial analyses of the acoustic properties for the standing plane wave and the Gaussian planar pulse show that the Cumulant LBM reproduces the dissipation and dispersion rates of the theoretical solutions. In general, the phase speed and dissipation errors are almost constant, even for a relatively low resolution mesh, and they are independent of viscosity and fluid regime, but a function of the number of

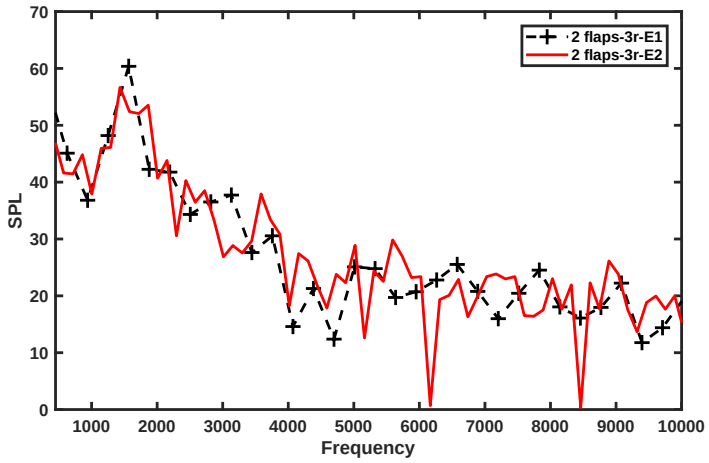

Figure 19: Sound pressure level [dB] as a function of frequency [Hz] for single cylinder case

points per wavelength.

The comparison with analytical solutions shows that the Cumulant LBM correctly reproduces the spherical acoustic pulse wave propagation, as well as the infinite spherical wave emitted from a point source. However, the BGK LBM has difficulties reproducing infinite spherical wave propagation. The solution displays chaotic behavior due to a numerical instability at low viscosities.

The FSI study of the effect of flaps on the vorticity and the frequency of the flow pattern using the Cumulant LBM ends up with the idea that the mobility of such flaps is one of the major factors altering the phase within the vortex shedding cycle. They reduce the transversal dislocation of the shed vorticity, causing the vortices being shed in a row along the center-line of the flow over a single cylinder.

As a final conclusion, the Cumulant LBM correctly predicts the aerodynamic, hydrodynamic, and acoustic characteristics of different phenomena at high Re and different flow regimes in a simple way without additional computational cost.

5. Acknowledgments

This work has been funded the Spanish Ministry of Economy, Industry and Competitiveness – Research National Agency (under project DPI2016-75791-C2-1-P), by FEDER funds and by Generalitat de Catalunya - AGAUR (under project 2017 SGR 01234)

6. Bibliography

[1] E. G. Richardson, Aeolian tones, Proceedings of the Physical Society of London 36 (1) (1923) 153–167. doi:10.1088/1478-7814/36/1/320.
URL https://doi.org/10.1088%2F1478-7814%2F36%2F1%2F320

[2] B. Etkin, G. K. Korbacher, R. T. Keefe, Acoustic radiation from a stationary cylinder in a fluid stream (aeolian tones), The Journal of the Acoustical Society of America 29 (1) (1957) 30–36. arXiv:https://doi.org/10.1121/1.1908673, doi:10.1121/1.1908673.
URL https://doi.org/10.1121/1.1908673

[3] R. Blevins, Review of sound induced by vortex shedding from cylinders, Journal of Sound and Vibration 92 (4) (1984) 455 – 470. doi:https://doi.org/10.1016/0022-460X(84)90191-3.
URL http://www.sciencedirect.com/science/article/pii/0022460X84901913

[4] W. K. Blake, Mechanics of flow-induced sound and vibration, Orlando, Fla. : Academic Press, 1986, includes bibliographies and index.

[5] C. Norberg, Fluctuating lift on a circular cylinder: review and new measurements 17 (1) (2003) 57–96.
URL http://dx.doi.org/10.1016/S0889-9746(02)00099-3

[6] V. Strouhal, Ueber eine besondere art der tonerregung, Annalen der Physik 241 (10) (1878) 216–251. arXiv:https://onlinelibrary.wiley.com/doi/pdf/10.1002/andp.18782411005, doi:10.1002/andp.18782411005.
URL https://onlinelibrary.wiley.com/doi/abs/10.1002/andp.18782411005

[7] J. C. Hardin, S. L. Lamkin, Aeroacoustic computation of cylinder wake flow., AIAA Journal 22 (1) (1984) 51–57. arXiv:https://doi.org/10.2514/3.48418, doi:10.2514/3.48418.
URL https://doi.org/10.2514/3.48418

[8] J. S. Cox, K. S. Brentner, C. L. Rumsey, Computation of vortex shedding and radiated sound for a circular cylinder: Subcritical to transcritical reynolds numbers, Theoretical and Computational Fluid Dynamics 12 (4) (1998) 233–253. doi:10.1007/s001620050108.
URL https://doi.org/10.1007/s001620050108

[9] O. Inoue, W. Iwakami, N. Hatakeyama, Aeolian tones radiated from flow past two square cylinders in a side-by-side arrangement, Physics of Fluids 18 (4) (2006) 046104. arXiv:https://doi.org/10.1063/1.2191847, doi:10.1063/1.2191847.
URL https://doi.org/10.1063/1.2191847

[10] C. K. W. Tam, Computational aeroacoustics - issues and methods, AIAA Journal 33 (10) (1995) 1788–1796. arXiv:https://doi.org/10.2514/3.12728, doi:10.2514/3.12728.
URL https://doi.org/10.2514/3.12728

[11] V. L. Wells, R. A. Renaut, Computing aerodynamically generated noise, Annual Review of Fluid Mechanics 29 (1) (1997) 161–199. arXiv:https://doi.org/10.1146/annurev.fluid.29.1.161, doi:10.1146/annurev.fluid.29.1.161.
URL https://doi.org/10.1146/annurev.fluid.29.1.161

[12] J. W. Kim, D. J. Lee, Optimized compact finite difference schemes with maximum resolution, AIAA Journal 34 (5) (1996) 887–893. arXiv:https://doi.org/10.2514/3.13164, doi:10.2514/3.13164.
URL https://doi.org/10.2514/3.13164

[13] S. K. Lele, Compact finite difference schemes with spectral-like resolution, in: Numerical Modeling of Seismic Wave

Propagation: Gridded Two-way Wave-equation Methods, Society of Exploration Geophysicists, 2012. doi:10.1190/1.9781560803089.

[14] C. K. Tam, J. C. Webb, Dispersion-relation-preserving schemes for computational aeroacoustics.

[15] C. Cheong, S. Lee, Grid-optimized dispersion-relation-preserving schemes on general geometries for computational aeroacoustics, Journal of Computational Physics 174 (1) (2001) 248 – 276. doi:https://doi.org/10.1006/jcph.2001.6904.
URL http://www.sciencedirect.com/science/article/pii/S0021999101969049

[16] M. Zdravkovich, Review and classification of various aerodynamic and hydrodynamic means for suppressing vortex shedding, Journal of Wind Engineering and Industrial Aerodynamics 7 (2) (1981) 145 – 189. doi:https://doi.org/10.1016/0167-6105(81)90036-2.
URL http://www.sciencedirect.com/science/article/pii/0167610581900362

[17] S.-J. Lee, H.-C. Lim, M. Han, S. S. Lee, Flow control of circular cylinder with a v-grooved micro-riblet film, Fluid Dynamics Research 37 (4) (2005) 246 – 266. doi:https://doi.org/10.1016/j.fluiddyn.2005.05.002.
URL http://www.sciencedirect.com/science/article/pii/S0169598305000717

[18] P. W. Bearman, Investigation of the flow behind a two-dimensional model with a blunt trailing edge and fitted with splitter plates, Journal of Fluid Mechanics 21 (2) (1965) 241–255. doi:10.1017/S0022112065000162.

[19] K. Kwon, H. Choi, Control of laminar vortex shedding behind a circular cylinder using splitter plates, Physics of Fluids 8 (2) (1996) 479–486. arXiv:https://doi.org/10.1063/1.868801, doi:10.1063/1.868801.
URL https://doi.org/10.1063/1.868801

[20] H. Akilli, C. Karakus, A. Akar, B. Sahin, N. Ozdil, Control of vortex shedding of circular cylinder in shallow water flow using an attached splitter plate, Journal of Fluids Engineering-transactions of The Asme - J FLUID ENG 130. doi:10.1115/1.2903813.

[21] N. Mazellier, A. Feuvrier, A. Kourta, Biomimetic bluff body drag reduction by self-adaptive porous flaps, Comptes Rendus Mécanique 340 (1) (2012) 81 – 94, biomimetic flow control. doi:https://doi.org/10.1016/j.crme.2011.11.006.
URL http://www.sciencedirect.com/science/article/pii/S1631072111001926

[22] S. Kunze, C. Brücker, Control of vortex shedding on a circular cylinder using self-adaptive hairy-flaps, Comptes Rendus Mécanique 340 (1) (2012) 41 – 56, biomimetic flow control. doi:https://doi.org/10.1016/j.crme.2011.11.009.
URL http://www.sciencedirect.com/science/article/pii/S1631072111001951

[23] L. Kamps, T. F. Geyer, E. Sarradj, C. Brücker, Vortex shedding noise of a cylinder with hairy flaps, Journal of Sound and Vibration 388 (2017) 69–84.

[24] T. Colonius, S. K. Lele, P. Moin, The scattering of sound waves by a vortex: numerical simulations and analytical solutions, Journal of Fluid Mechanics 260 (1994) 271–298. doi:10.1017/S0022112094003514.

[25] B. MITCHELL, S. LELE, P. MOIN, Direct computation of the sound from a compressible co-rotating vortex pair. arXiv:https://arc.aiaa.org/doi/pdf/10.2514/6.1992-374, doi:10.2514/6.1992-374.
URL https://arc.aiaa.org/doi/abs/10.2514/6.1992-374

[26] O. INOUE, N. HATAKEYAMA, Sound generation by a two-dimensional circular cylinder in a uniform flow, Journal of Fluid Mechanics 471 (2002) 285–314. doi:10.1017/S0022112002002124.

[27] E. G. Fard, A cumulant lbm approach for large eddy simulation of dispersion microsystems, Ph.D. thesis, Univ.-Bibl. (2015).

[28] E. Kian Far, M. Geier, K. Kutscher, M. Krafczyk, Implicit large eddy simulation of flow in a micro-orifice with the

cumulant lattice boltzmann method, Computation 5 (2). doi:10.3390/computation5020023.
URL https://www.mdpi.com/2079-3197/5/2/23

[29] J. Buick, C. Greated, D. Campbell, Lattice bgk simulation of sound waves, EPL (Europhysics Letters) 43 (3) (1998) 235.

[30] P. J. Dellar, Bulk and shear viscosities in lattice boltzmann equations, Physical Review E 64 (3) (2001) 031203.

[31] B. Crouse, D. Freed, G. Balasubramanian, S. Senthooran, P. Lew, L. Mongeau, Fundamental aeroacoustic capabilities of the lattice-boltzmann method, 12th aiaa, in: CEAS Aeroacoustics Conference and Exhibit, AIAA, 2006, pp. 06–2571.

[32] S. Marié, D. Ricot, P. Sagaut, Comparison between lattice boltzmann method and navier–stokes high order schemes for computational aeroacoustics, Journal of Computational Physics 228 (4) (2009) 1056–1070.

[33] G. Brès, F. Pérot, D. Freed, Properties of the lattice boltzmann method for acoustics, in: 15th AIAA/CEAS Aeroacoustics Conference (30th AIAA Aeroacoustics Conference), 2009, p. 3395.

[34] E. M. Viggen, The lattice boltzmann method: Fundamentals and acoustics.

[35] D. B. Dhuri, S. M. Hanasoge, P. Perlekar, J. O. Robertsson, Numerical analysis of the lattice boltzmann method for simulation of linear acoustic waves, Physical Review E 95 (4) (2017) 043306.

[36] T. Kataoka, M. Tsutahara, Lattice boltzmann model for the compressible navier-stokes equations with flexible specific-heat ratio, Phys. Rev. E 69 (2004) 035701. doi:10.1103/PhysRevE.69.035701.
URL https://link.aps.org/doi/10.1103/PhysRevE.69.035701

[37] M. Watari, M. Tsutahara, Two-dimensional thermal model of the finite-difference lattice boltzmann method with high spatial isotropy, Phys. Rev. E 67 (2003) 036306. doi:10.1103/PhysRevE.67.036306.
URL https://link.aps.org/doi/10.1103/PhysRevE.67.036306

[38] H.-M. Noh, Numerical analysis of aerodynamic noise from pantograph in high-speed trains using lattice boltzmann method, Advances in Mechanical Engineering 11 (7) (2019) 1687814019863995.

[39] F. Dubois, P. Lallemand, Quartic parameters for acoustic applications of lattice boltzmann scheme, Computers & Mathematics with Applications 61 (12) (2011) 3404–3416.

[40] F. Dubois, Stable lattice boltzmann schemes with a dual entropy approach for monodimensional nonlinear waves, Computers & Mathematics with Applications 65 (2) (2013) 142–159.

[41] Y. Li, R. Shock, R. Zhang, H. Chen, Numerical study of flow past an impulsively started cylinder by the lattice-boltzmann method, Journal of Fluid Mechanics 519 (2004) 273.

[42] D. Ricot, S. Marié, P. Sagaut, C. Bailly, Lattice boltzmann method with selective viscosity filter, Journal of Computational Physics 228 (12) (2009) 4478–4490.

[43] P. Lallemand, L.-S. Luo, Theory of the lattice boltzmann method: Dispersion, dissipation, isotropy, galilean invariance, and stability, Physical Review E 61 (6) (2000) 6546.

[44] H. Xu, P. Sagaut, Optimal low-dispersion low-dissipation lbm schemes for computational aeroacoustics, Journal of Computational Physics 230 (13) (2011) 5353–5382.

[45] P. J. Dellar, Lattice boltzmann algorithms without cubic defects in galilean invariance on standard lattices, Journal of Computational Physics 259 (2014) 270–283.

[46] Y.-H. Qian, Fractional propagation and the elimination of staggered invariants in lattice-bgk models, International journal of modern physics C 8 (04) (1997) 753–761.

[47] H. Fan, R. Zhang, H. Chen, Extended volumetric scheme for lattice boltzmann models, Physical Review E 73 (6) (2006) 066708.

[48] X. Niu, C. Shu, Y. Chew, T. Wang, Investigation of stability and hydrodynamics of different lattice boltzmann models, Journal of statistical physics 117 (3-4) (2004) 665–680.

[49] S. Ansumali, I. V. Karlin, Single relaxation time model for entropic lattice boltzmann methods, Physical Review E 65 (5) (2002) 056312.

[50] R. Brownlee, A. N. Gorban, J. Levesley, Stabilization of the lattice boltzmann method using the ehrenfests' coarse-graining idea, Physical Review E 74 (3) (2006) 037703.

[51] R. Brownlee, A. N. Gorban, J. Levesley, Stability and stabilization of the lattice boltzmann method, Physical Review E 75 (3) (2007) 036711.

[52] R. Brownlee, A. N. Gorban, J. Levesley, Nonequilibrium entropy limiters in lattice boltzmann methods, Physica A: Statistical Mechanics and its Applications 387 (2-3) (2008) 385–406.

[53] J. Latt, B. Chopard, Lattice boltzmann method with regularized pre-collision distribution functions, Mathematics and Computers in Simulation 72 (2-6) (2006) 165–168.

[54] O. Malaspinas, Increasing stability and accuracy of the lattice boltzmann scheme: recursivity and regularization, arXiv preprint arXiv:1505.06900.

[55] F. Brogi, O. Malaspinas, B. Chopard, C. Bonadonna, Hermite regularization of the lattice boltzmann method for open source computational aeroacoustics, The Journal of the Acoustical Society of America 142 (4) (2017) 2332–2345.

[56] E. Kian Far, M. Geier, K. Kutscher, M. Konstantin, Simulation of micro aggregate breakage in turbulent flows by the cumulant lattice boltzmann method, Computers & Fluids 140 (2016) 222 – 231. doi:https://doi.org/10.1016/j.compfluid.2016.10.001.
URL http://www.sciencedirect.com/science/article/pii/S0045793016302936

[57] E. Kian Far, S. Langer, Analysis of the cumulant lattice boltzmann method for acoustics problems, in: the 13th International Conference on Theoretical and Computational Acoustics At: Vienna, Austria, 2017.

[58] E. Kian Far, M. Geier, M. Krafczyk, Simulation of rotating objects in fluids with the cumulant lattice boltzmann model on sliding meshes, Computers & Mathematics with Applicationsdoi:https://doi.org/10.1016/j.camwa.2018.08.055.
URL http://www.sciencedirect.com/science/article/pii/S0898122118304814

[59] M. Gorakifard, C. Salueña, I. Cuesta, E. Kian Far, Acoustical analysis of fluid structure interaction using the cumulant lattice boltzmann method, in: The 16th International Conference for Mesoscopic Methods in Engineering and Science At: Heriot-Watt University, Edinburgh, Scotland, 2019.

[60] C. G. Coreixas, High-order extension of the recursive regularized lattice boltzmann method, Ph.D. thesis (2018).

[61] C. Coreixas, G. Wissocq, G. Puigt, J.-F. Boussuge, P. Sagaut, Recursive regularization step for high-order lattice boltzmann methods, Physical Review E 96 (3) (2017) 033306.

[62] Y. Feng, P. Boivin, J. Jacob, P. Sagaut, Hybrid recursive regularized thermal lattice boltzmann model for high subsonic compressible flows, Journal of Computational Physics 394 (2019) 82–99.

[63] E. Kian Far, M. Geier, K. Kutscher, M. Krafczyk, Distributed cumulant lattice boltzmann simulation of the dispersion process of ceramic agglomerates, Journal of Computational Methods in Sciences and Engineering 16 (2) (2016) 231–252.

[64] M. Geier, M. Schönherr, A. Pasquali, M. Krafczyk, The cumulant lattice boltzmann equation in three dimensions: Theory and validation, Computers & Mathematics with Applications 70 (4) (2015) 507–547.

[65] A. Pasquali, M. Geier, M. Krafczyk, Near-wall treatment for the simulation of turbulent flow by the cumulant lattice boltzmann method, Computers & Mathematics with Applications 79 (1) (2020) 195–212.

[66] J. N. Reddy, An introduction to the finite element method, New York 27.

[67] E. Kian Far, Simulation of moving body in field flow and fluid structure interaction with using lattice boltzmann method, Ph.D. thesis (05 2010).

[68] E. G. Fard, E. Shirani, S. Geller, The fluid structure interaction with using of lattice boltzmann method.

[69] S. Geller, J. Tölke, M. Krafczyk, Lattice-boltzmann method on quadtree-type grids for fluid-structure interaction, in: Fluid-Structure Interaction, Springer, 2006, pp. 270–293.

[70] R. Mei, D. Yu, W. Shyy, L.-S. Luo, Force evaluation in the lattice boltzmann method involving curved geometry, Physical Review E 65 (4) (2002) 041203.

[71] W. E. Lorensen, H. E. Cline, Marching cubes: A high resolution 3d surface construction algorithm, ACM siggraph computer graphics 21 (4) (1987) 163–169.

[72] L. Luo, Consistent initial conditions for lbe simulation, preprint.

[73] P. M. Morse, H. Feshbach, Methods of theoretical physics, American Journal of Physics 22 (6) (1954) 410–413.

[74] L. E. Kinsler, A. R. Frey, A. B. Coppens, J. V. Sanders, Fundamentals of acoustics, Fundamentals of Acoustics, 4th Edition, by Lawrence E. Kinsler, Austin R. Frey, Alan B. Coppens, James V. Sanders, pp. 560. ISBN 0-471-84789-5. Wiley-VCH, December 1999. (1999) 560.

[75] E. M. Viggen, The lattice boltzmann method with applications in acoustics, Master's thesis, Norges teknisk-naturvitenskapelige universitet, Fakultet for naturvitenskap … (2009).

[76] F. Gendre, D. Ricot, G. Fritz, P. Sagaut, Grid refinement for aeroacoustics in the lattice boltzmann method: A directional splitting approach, Physical Review E 96 (2) (2017) 023311.

[77] C. K. Tam, J. C. Webb, Dispersion-relation-preserving finite difference schemes for computational acoustics, Journal of computational physics 107 (2) (1993) 262–281.

[78] E. M. Salomons, W. J. Lohman, H. Zhou, Simulation of sound waves using the lattice boltzmann method for fluid flow: Benchmark cases for outdoor sound propagation, PloS one 11 (1) (2016) e0147206.

[79] E. Vergnault, O. Malaspinas, P. Sagaut, Noise source identification with the lattice boltzmann method, The Journal of the Acoustical Society of America 133 (3) (2013) 1293–1305.

[80] M. Bouzidi, M. Firdaouss, P. Lallemand, Momentum transfer of a boltzmann-lattice fluid with boundaries, Physics of fluids 13 (11) (2001) 3452–3459.

[81] P. Lallemand, L.-S. Luo, Lattice boltzmann method for moving boundaries, Journal of Computational Physics 184 (2) (2003) 406–421.

[82] J. Lienhard, L. Liu, Locked-in vortex shedding behind oscillating circular cylinders, with application to transmission lines, Citeseer, 1967.

[83] E. Achenbach, E. Heinecke, On vortex shedding from smooth and rough cylinders in the range of reynolds numbers 6× 10 3 to 5× 10 6, Journal of fluid mechanics 109 (1981) 239–251.

[84] M. D. Dahl, Fourth computational aeroacoustics (caa) workshop on benchmark problems.

[85] M. Kiya, M. Arie, H. Tamura, H. Mori, Vortex shedding from two circular cylinders in staggered arrangement.

[86] C. Cheong, J. Ryu, S. Lee, Computation of aeolian tones from twin-cylinders using immersed surface dipole sources, Journal of mechanical science and technology 20 (12) (2006) 2292–2314.